Alma Mater Studiorum · Università di Bologna

Scuola di Scienze
Corso di Laurea Magistrale in Fisica

PERFORMANCE ANALYSIS OF RECONSTRUCTION ALGORITHMS FOR BREAST MICROWAVE IMAGING

Relatore:
Prof. NICO LANCONELLI

Presentata da:
FRANCESCO PAREO

Correlatori:
PhD. SIMONE MASETTI
Dr. MASSIMILIANO GRANDI

Sessione I
Anno Accademico 2015/2016

"Chi ha occhio, trova quel che cerca anche ad occhi chiusi."

Calvino, Italo. Marcovaldo. Edizioni Mondadori, 2012.

Sommario

Nella presente tesi è sviluppato ed analizzato il problema della localizzazione di uno scatteratore posto in un dominio circolare omogeneo. Tale problema è alla base dello studio di un possibile metodo di screening al seno basato sull'imaging a microonde, in cui lo scatteratore rappresenta il tumore ed il domino circolare, il seno.

L'imaging a microonde include diverse tecniche per la rilevazione, localizzazione e caratterizzazione di tumori al seno. L'impiego di ciascuna di queste tecniche implica la risoluzione di un problema di scattering inverso. Nel problema considerato (localizzazione del target) la soluzione al problema di scattering inverso è ricavata attraverso un algoritmo di ricostruzione basato su un modello di linearizzaione della soluzione e ispirato agli algoritmi: MUoltiple SIgnal Classification (MUSIC) e Time Reversal (TR). L'algoritmo d'imaging implementato restituisce un'immagine in cui è ricostruito il dominio circolare e, se presente, è rilevato lo scatteratore. Tale immagine è chiamata pseudospettro. Attraverso un'analisi preliminare delle prestazioni dell'algoritmo al variare della frequenza di lavoro utilizzata, è osservato che le performance di risoluzione e rapporto segnale-rumore dell'algoritmo accrescono se si combinano i risultati delle immagini a singola frequenza. A tal scopo è proposto un nuovo metodo di combinazione a multifrequenza chiamato: Geometric Mean-MUSIC algorithm (GM-MUSIC). L'algoritmo GM-MUSIC è testato in diverse circostanze variando i seguenti parametri: posizione del tumore, dimensione del tumore, dimensione del seno e proprietà elettriche del seno. I dati utilizzati per le ricostruzioni sono stati ricavati da precedenti simulazioni al computer. L'analisi condotta sulle performance dell'algoritmo rivela che: il GM-MUSIC localizza lo scatterer finché i parametri elettrici del seno sono noti. Questo è un limite evidente, dal momento che, in una situazione reale, l'anatomia del seno è generalmente sconosciuta. Nel progetto di tesi è proposta una possibile soluzione attraverso l'algoritmo Eye-GMMUSIC. L'Eye-GMMUSIC è un algoritmo di ottimizzazione basato sull'algoritmo pattern search: esso cerca i parametri elettrici del seno che minimizzano il rapporto segnale-rumore e poi ricostruisce l'immagine con i parametri trovati.

Infine, gli algoritmi GM-MUSIC ed Eye-GMMUSIC sono testati su dati sperimentati ricavati con un sistema d'imaging a microonde composito di un'antenna a dipolo, un Vector Network Analyzer e un

seno-prototipo costruito all'Università di Bologna. Dalle ricostruzioni ottenute con i risultati sperimentali, si conclude che l'algoritmo GM-MUSIC rileva la posizione dello scatteratore all'interno del fantoccio.

Abstract

The problem of localizing a scatterer, which represents a tumor, in a homogeneous circular domain, which represents a breast, is addressed. A breast imaging method based on microwaves is considered.

The microwave imaging involves to several techniques for detecting, localizing and characterizing tumors in breast tissues. In all such methods an electromagnetic inverse scattering problem exists. For the scattering detection method, an algorithm based on a linear procedure solution, inspired by MUltiple SIgnal Classification algorithm (MUSIC) and Time Reversal method (TR), is implemented. The algorithm returns a reconstructed image of the investigation domain in which it is detected the scatterer position. This image is called pseudospectrum.

A preliminary performance analysis of the algorithm vying the working frequency is performed: the resolution and the signal-to-noise ratio of the pseudospectra are improved if a multi-frequency approach is considered. The Geometrical Mean-MUSIC algorithm (GM- MUSIC) is proposed as multi-frequency method. The performance of the GM-MUSIC is tested in different real life computer simulations. The performed analysis shows that the algorithm detects the scatterer until the electrical parameters of the breast are known. This is an evident limit, since, in a real life situation, the anatomy of the breast is unknown. An improvement in GM-MUSIC is proposed: the Eye-GMMUSIC algorithm. Eye-GMMUSIC algorithm needs no a priori information on the electrical parameters of the breast. It is an optimizing algorithm based on the pattern search algorithm: it searches the breast parameters which minimize the Signal-to-Clutter Mean Ratio (SCMR) in the signal.

Finally, the GM-MUSIC and the Eye-GMMUSIC algorithms are tested on a microwave breast cancer detection system consisting of an dipole antenna, a Vector Network Analyzer and a novel breast phantom built at University of Bologna. The reconstruction of the experimental data confirm the GM-MUSIC ability to localize a scatterer in a homogeneous medium.

Contents

Nomenclature **3**

1 Motivation **5**
1.1 Breast Cancer Statistics 5
1.2 Breast Screening Methods 7
1.2.1 Mammography 7
1.2.2 Breast MRI 9
1.2.3 Breast Ultrasound 9
1.3 Basics of Microwave Imaging 9
1.3.1 Electromagnetic Properties of Breast Tissue 10
1.3.2 A complex problem 13

2 Reconstruction Algorithm **15**
2.1 Physical Principles 15
2.2 Inverse Scattering Problem 16
2.2.1 Non-Linear Inverse scattering 17
2.2.2 Linear Inverse scattering 17
2.3 Time Reversal-MUSIC 18
2.3.1 Time Reversal Imaging 18
2.3.2 MUSIC Algorithm 20
2.3.3 MUSIC in monostatic configuration 21
2.3.4 GM-MUSIC Algorithm 22
2.4 Reconstruction Process 22
2.4.1 Clutter Cancellation 23
2.4.2 Assessment of scattering scenario 23
2.4.3 Evaluation of the reconstruction 26

3 Scatterer Detection **29**
3.1 Simulation Process 29
3.1.1 Finite element method 29
3.1.2 COMSOL-Multiphysics 30
3.2 The Operating Point 33
3.2.1 Working Frequency 34
3.2.2 Tumor Position 39
3.2.3 Tumor Size 40
3.2.4 Tumor-Background Contrast 41
3.2.5 Breast Size 42

3.2.6 Unknown Breast Properties 43
3.3 Unknown Parameter Solution 44
3.3.1 The Optimizing Algorithms Choice 45
3.3.2 Pattern Search Method 46
3.3.3 The Cost Function 47
3.3.4 The Eye-GMMUSIC algorithm 49
3.3.5 The Eye-GMMUSIC Results 49

4 Experimental Measurements **53**
4.1 The experimental setup 53
4.1.1 The breast phantom 53
4.1.2 The dipole antenna 55
4.1.3 Vector Network analyzer 56
4.1.4 PC and Software 58
4.2 Measures in air 59
4.3 Measures in oil 60
4.3.1 Measure in oil with alcohol scatterer 62
4.4 Eye-GMUSIC Results 63

5 Conclusions **65**

A Green function **67**

B Hankel function **69**

Nomenclature

Acronyms

ACR	American College of Rheumatology
BC	Boundary Condition
DOF	Degree Of Freedom
DUT	Device Under Test
FDTD	Finite-Difference Time-Domain
FEM	Finite Element Method
FWHM	Full Width at Half Maximum
GM-MUSIC	Geometrical Mean MUSIC
GUI	Graphical User Interface
I-MUSIC	Interferometric MUSIC
MoSR	Monostatic Response
MRI	Magnetic Resonance Imaging
MSR	Multistatic Response
MUSIC	MUltiple SIgnal Classification
ODE	Ordinary Differential Equation
PCA	Principal Component Analysis
PLM	Perfect Matched Layer
SCMR	Signal-to-Clutter Mean Ratio
SCR	Signal-to-Clutter Ratio
SD	Spatial Displacement

SNR	Signal-to-Noise Ratio
TR	Time Reversal
TRM	Time Reversal Matrix
TRX	Transceiver
VNA	Vector Network Analyzer
WB-MUSIC	WideBand MUSIC

Symbols

$\Delta\varepsilon$	Difference between ε_s and ε_∞	u.a.
ν	Frequency	Hz
$\overline{x}$	Mean Value	-
ϕ	Angular direction	-
ρ	Radial direction	-
σ	Conductivity	$\mathrm{S} \cdot \mathrm{m}^{-1}$
σ_x	Standard deviation	-
τ	Relaxation time	ps
ε	Relative permittivity	u.a.
$\varepsilon_0 = 8.854\ldots \cdot 10^{-12}$	Vacuum permittivity	$\mathrm{F} \cdot \mathrm{m}^{-1}$
ε_∞	Relative permittivity at frequencies $j2\pi f\tau \gg 1$	u.a.
ε_s	Relative permittivity at frequencies $j2\pi f\tau \ll 1$	u.a.
$c = 299792458$	Light speed	$\mathrm{m} \cdot \mathrm{s}^{-1}$
$j = \sqrt{-1}$	Complex index	-
se	Standard error	-

Chapter 1

Motivation

Breast cancer is the most frequently diagnosed cancer and the leading cause of cancer death in females worldwide. The most important prerequisite for a quick and effective treatment of the cancer is early detection. In recent years, prevention protocols are increasing in many states and research activities are focusing on breast screening, for this reason.

The primary screening method is X-ray mammography. Despite its recognized value in detecting and characterizing breast disease, X-ray mammography has important limitations that motivate the quest for alternatives to augment the diagnostic tools that are currently available to the radiologist.

In this thesis we concern about a new screening technique based on electromagnetic waves in the microwave frequency range. Over the last decade, increasing number of research groups have proposed microwave imaging as suitable method for breast cancer screening, because they hypothesize a noticeable contrast between normal and malignant breast tissues, notably superior to X-ray mammography.

1.1 Breast Cancer Statistics

The global burden of cancer continues to increase largely because of the aging and growth of the world population alongside an increasing adoption of cancer-causing behaviours (smoking, physical inactivity and unregulated diets). According to GLOBOCAN 2012 [1] an estimated 14.1 million new cancer cases and 8.2 million cancer-related deaths occurred in 2012, compared with 12.7 million and 7.6 million, respectively, in 2008. The most commonly diagnosed cancers worldwide are those of the lung (1.8 million, 13.0% of the total), breast (1.7 million, 11.9%), and colorectum (1.4 million, 9.7%). The most common causes of cancer death are cancers of the lung (1.6 million, 19.4% of the total), liver (0.8 million, 9.1%), and stomach (0.7 million, 8.8%), see Figure 1.1a .

Breast cancer is the most frequently diagnosed cancer and the leading cause of cancer death in females worldwide, accounting for 25% (1.7 million) of the total cancer cases and 15% (0.5 million) of the total cancer deaths, see Figure 1.1b. In Italy, the breast cancer affects one in a eight women, it is the most common cancer in women and accounts for 29% of the woman cancer cases, and 13% of the total cancer cases [2].

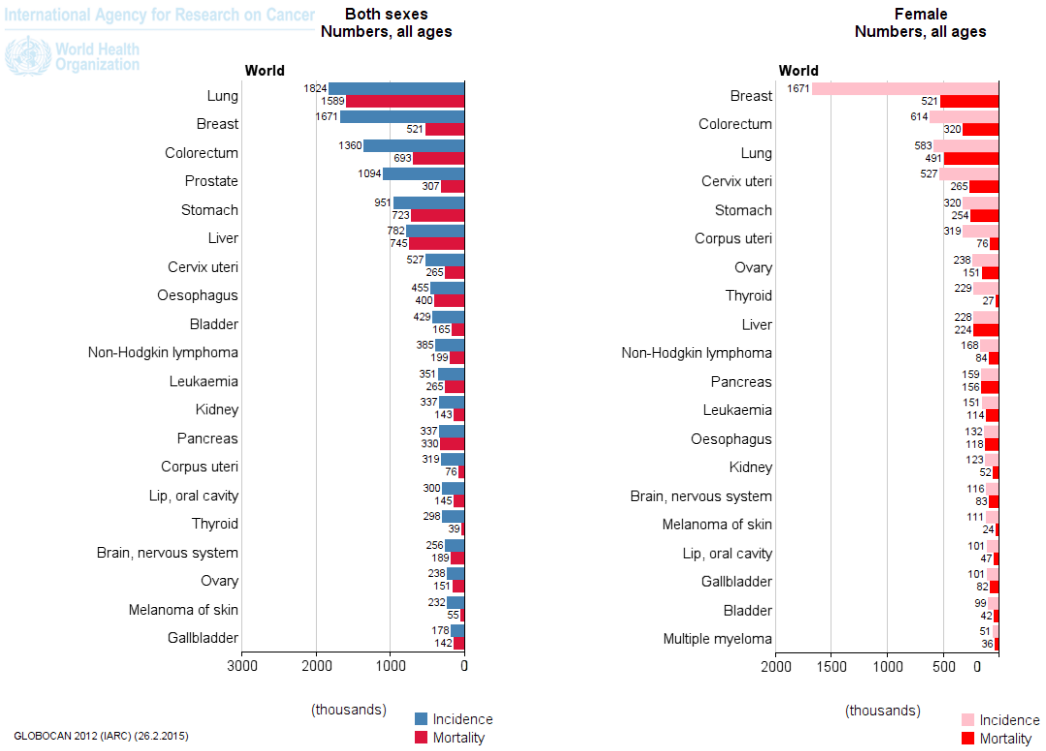

(a) **(b)**

Figure 1.1: (a) Cancer Incidence and Mortality Rates by World Area, all ages. (b) Female gender only. Source: GLOBOCAN, 2012 [1].

Figures 1.2a and 1.2b shows the estimated number of female breast cancer cases and deaths occurred in the United States since 1975 to 2008 by age. Much of the historic increase in invasive breast cancer incidence in the early 1980s reflects the increased diagnoses due to the introduction of mammography screening as well as changes in reproductive patterns.

Figure 1.2c also shows trends in death rates for breast cancer by age at death. After slowly increasing for many years (1975-1990), breast cancer death rates decreased by 2.2% per year from 1990 to 2007 for women of all ages combined. The decline is larger among women aged younger than 50 years than among those aged 50 years and older. Declines in breast cancer mortality have been attributed to both improvements in treatment and early detection [3].

It follows that the most important prerequisite for a quick and effective treatment of the cancer is early detection. Early detection and treatment of breast cancer can arrest disease progression, decrease the rate of advanced cancers, and reduce breast cancer mortality in the screened population. When high quality breast screening is offered at regular intervals from 40- to 74-year-old women, over 50% of the invasive cancers will be detected in the size range of 1-14mm, fewer than 20% will be axillary node positive, and only about 20% will be poorly differentiated [4].

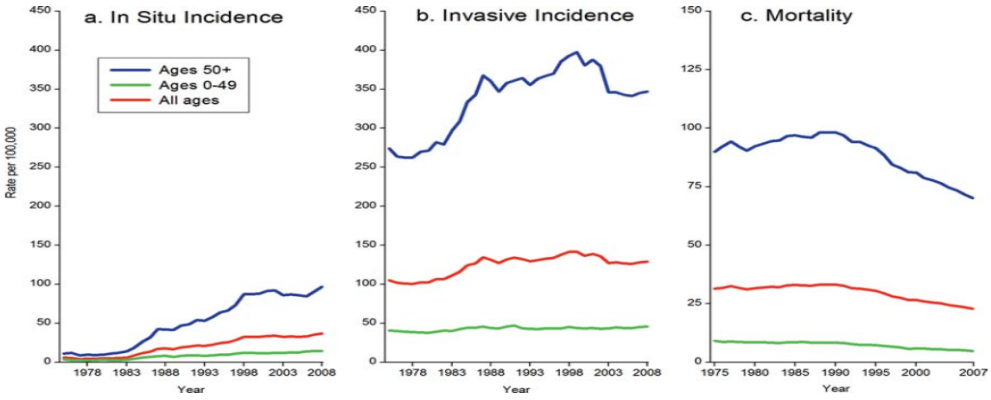

Figure 1.2: Incidence and Mortality Rates of Female Breast Cancer by Age, United States, 1975 to 2008 [3].

1.2 Breast Screening Methods

Breast cancer screening is the medical screening of asymptomatic and apparently healthy women for breast cancer in an attempt to achieve an earlier diagnosis. The assumption is that early detection will improve outcomes. A number of screening tests have been employed, including clinical and self breast exams, mammography, ultrasound, and magnetic resonance imaging.

A clinical or self breast exam involves feeling the breast for lumps or other abnormalities. These tests are recommended and bring benefits in the prevention of breast cancer. Medical evidence, however, does not support its use in women with a typical risk for breast cancer, so they must to be corroborated by more accurate screening tests.

1.2.1 Mammography

The gold standard breast screening method is X-ray mammography. Mammography is a noninvasive medical test which uses low-energy X-rays, usually around 20 keV, to examine the human breast. The X-rays mammography involves exposing the breast to a small dose (about 0.4 mSv) of ionizing radiation. Equipment for mammography has evolved over at least the last 40 years to the current state of the art. While there are some differences from one manufacturer to another, there are also many characteristics and features that are common to all, see Figure 1.3:

- X-ray Tube Anode: mammography equipment uses molybdenum as the anode material or in some designs, a dual material anode with an additional rhodium track, they produce a characteristic radiation spectrum that is close to optimum for breast imaging.
- Filter: whereas most x-ray machines use aluminium or "aluminium equivalent" to filter the x-ray beam to reduce unnecessary exposure to the patient, in addition mammography uses molybdenum filters to enhance contrast sensitivity.
- Focal Spots: the typical x-ray tube for mammography has two selectable focal spots. The spots are generally smaller than for other x-ray procedures

because of the requirements for minimal blurring and good visibility of detail to see the small calcifications. The smaller of the two spots is generally used for the magnification technique.

- Compression: good compression of the breast is one of the essentials of effective mammography (and a common source of patient discomfort and concern). Potential benefits derived from compression include: a more uniform breast thickness resulting in a better fit of the exposure into the film latitude or dynamic range; reduced blurring from patient motion; reduced scattered radiation and improved contrast sensitivity; reduced radiation dose; better visualization of tissues near the chest wall.
- Grid: a grid is used in mammography (as in other x-ray procedures) to absorb scattered radiation and improve contrast sensitivity.
- Receptor: Both film/screen and digital receptors are used for mammography. Each has special characteristics to enhance image quality.

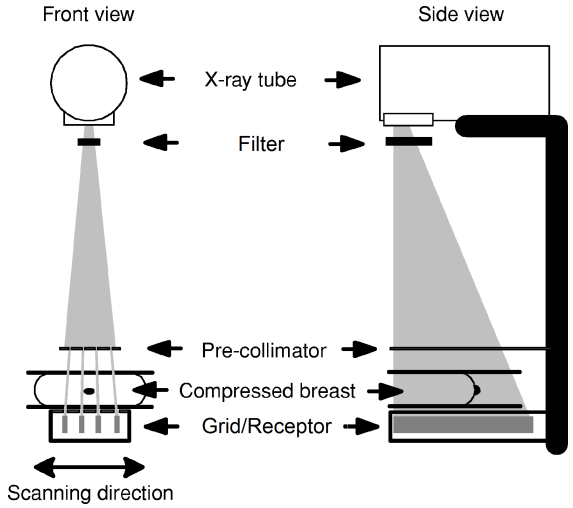

Figure 1.3: A schematic mammography system with its principal components.

Mammography has the following advantages: it is a relatively low-cost exam, it can be performed by nurses and it lasts about 10 minutes. Yet mammography suffers from its own limitations. First, the rate of failure of mammography in detecting breast cancer, termed false negative, is relatively high and can range from 4% to as high as 34% [5]. In a large-scale study, a total of 9762 screening mammograms were performed, for a median of 4 mammograms per woman over the 10-year period. Of the women who were screened, 23.8% had at least one false positive mammogram and the estimated cumulative risk of a false positive result was 49.1% after 10 mammograms [6]. There is also the burden of the X-ray absorbed dose: the ionizing X-ray in mammography poses a serious health risk to women and can even increase the chance for cancer development [7]. Moreover, mammography can provide an high degree of discomfort to the patient due to the breast compression which is often painful.

1.2.2 Breast MRI

The shortcomings of X-ray mammography imply that there is room for complementary imaging modalities. One alternative to mammography is Breast-MRI (or contrast enhanced Magnetic Resonance Imaging), it has shown substantial progress in the detection of breast cancer. In this method, the breast is scanned in an MRI device before and after the intravascular injection of a contrast agent (Gadolinium DTPA). The pre-contrast images are "subtracted" from the post-contrast images, and any areas that have increased blood flow are seen as bright spots on a dark background. Since breast cancers generally have an increased blood supply, the contrast agent causes these lesions to "light up" on the images. MRI techniques offers higher sensitivity which should be traded-off with high cost and low specificity, therefore, MRI is not currently used for breast cancer screening except for high risk case [8].

1.2.3 Breast Ultrasound

Ultrasound techniques has also been used in breast cancer detection. Ultrasound imaging, also called ultrasound scanning or sonography, involves the use of a small transducer (probe) and ultrasound gel placed directly on the skin. High-frequency sound waves (greater than 20KHz) are transmitted from the probe through the gel into the body. The ultrasound wave travels through different tissues at different rates of speed. The point at which adjacent tissues with different speeds of sound meet is referred to as an acoustic interface. When sound hits an acoustic interface, an echo is created. The transducer collects the sounds that bounce back and a computer then uses sound waves to create an image. The ultrasound advantages are: painless exam, non-ionizing radiation thus there is no radiation exposure to the patient, real-time images than they can show the structure and movement of the body's internal organs, as well as blood flowing through blood vessels. Ultrasound has also been used in breast cancer detection with a false negative rate of 17/100 and also requires highly specialized doctors to perform the exams. [9].

In this thesis, we will be concerned on the method based on electromagnetic waves in the region of microwave frequency: Microwave Imaging. An imaging method based on microwaves is non-ionizing, painless to the patient and cheaper than X-ray and MRI screening systems. Microwave imaging is discussed in next section more in detail.

1.3 Basics of Microwave Imaging

Since the pioneering work of Larsen and Jacobi (1978) [10], there has been a great excitement and research activities around microwave imaging for breast cancer detection, and in recent years an increasing number of research groups have proposed microwave imaging as an imaging modality suitable for breast cancer detection. This is because a microwave method uses non-ionizing radiation, the need for breast compression is eliminated and the cost of the exam is lower than

X-ray and MRI systems. Moreover, Hagness et al. [11–13] hypothesize that in the range of microwave frequencies there is a large contrast between normal and malignant breast tissues, superior to the radiographic density exploited by X-ray mammography.

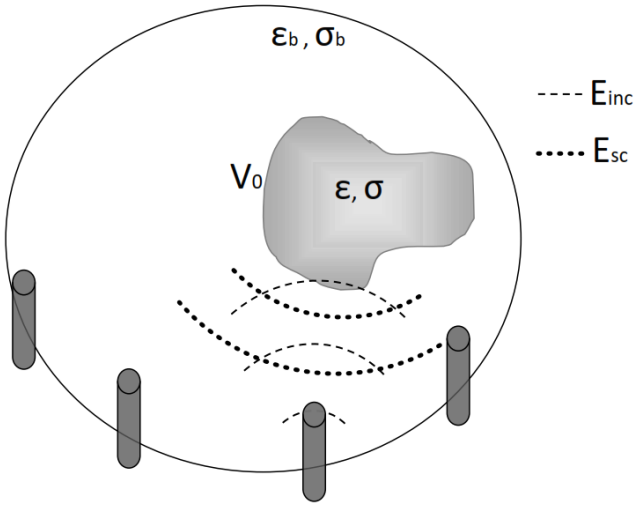

Figure 1.4: Schematized microwave imaging system. A system of antennas irradiate a medium with ϵ_b and σ_b, in which is embedded a target with ϵ and σ.

More in detail, microwave imaging is based on the fact that an inhomogeneity in the constitutive electromagnetic parameters (permittivity and conductivity) of a material will cause an incident electromagnetic field to scatter. A schematic of a microwave imaging system is shown in Fig. 1.4. The background medium, in which the microwave imaging system is embedded, is characterized by the permittivity ϵ_b and conductivity σ_b and the circular area in the center of the antenna group represents the imaging domain. This domain is irradiated by a transmitting antenna and the total field may be measured by one or more antennas positioned outside the domain. When an object with contrast in the constitutive parameters is positioned inside the imaging domain, a scattered field will arise. The total field, measured by the receiving antennas, is the sum of the incident field and the scattered field:

$$E_{tot} = E_{inc} + E_{sc} \tag{1.1}$$

thus the field changes when a scattered is introduced. From this change in the measured field, information about the location and/or constitutive parameters of the scattering object, also known as the scatterer, may be obtained.

1.3.1 Electromagnetic Properties of Breast Tissue

In this section the dielectric properties of human breast tissues are introduced to understand the principles of microwave imaging. A brief description of the definition and the widely used model for the dispersion (frequency dependence) of the tissues are submitted, in addiction typical values of the dielectric properties of normal breast tissue and cancer tissue are given.

In microwave imaging the dielectric properties are reconstructed regarding the differences in the complex permittivity, while non-metallic materials are considered in biomedical applications, defined as:

$$\varepsilon_r = \varepsilon' - j\varepsilon'' \tag{1.2}$$

where $j = \sqrt{-1}$ is imaginary unit, ϵ' describing the polarization effects of charged particles in the tissue and ϵ'' describing the out-of-phase losses due to the displacement currents generated by the applied electromagnetic field. Considering the biological tissues as dielectrics, the losses often are described by the conduction σ, which is approximated to the displacement current effect only, as:

$$\sigma = 2\pi\nu\varepsilon_0\varepsilon'' \tag{1.3}$$

where is ε_0 the permittivity of free space and ν is the frequency. The dielectric properties are determined as ε' and ε'', or ε' and σ,

$$\varepsilon_r = \varepsilon' - j\frac{\sigma}{\varepsilon_0 2\pi\nu} \tag{1.4}$$

as function of frequency.

Some biological molecules are polar, e.g., water and many proteins. Permanent dipoles are randomly oriented, but if an external electric field is applied, they will reorient statistically. Induced dipoles will have the direction of the applied field. The orientation of polar molecules in an applied electric field requires time and, hence, causes a dispersion of the type given in Eq. (1.5), which is valid for any one time constant relaxation mechanism. However, a distribution of time constants will often be found due to molecular inhomogeneity and nonspherical shape. The time constant is proportional to the cube of the radius of the molecules, and typical characteristic frequencies are, e.g., 15-20 GHz for water and 400-500 MHz for simple amino acids. Proteins add another dispersion typically centered in the 1-10 MHz range [14]. In the microwave region the dominant relaxation is the dipolar relaxation of free water molecules. Therefore, the dielectric properties of the tissues in microwave region are highly correlated to the water content.

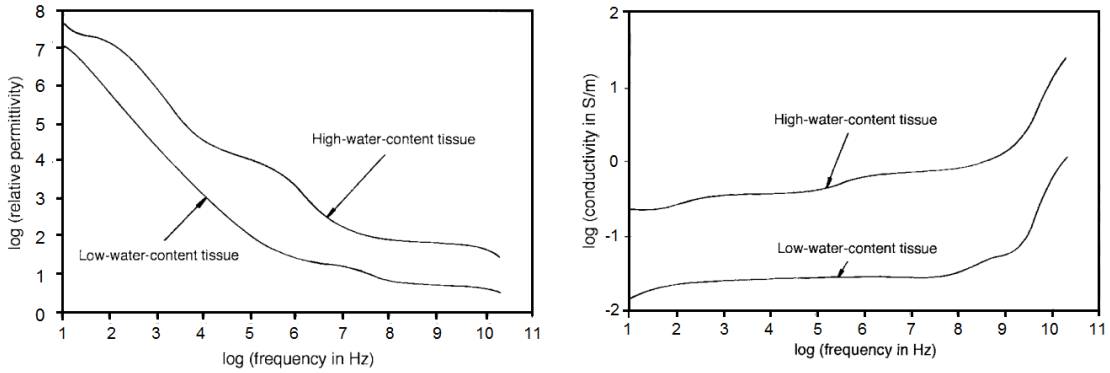

Figure 1.5: Comparison of the conductivity of high-water-content tissue such as muscle with low-water-content tissue such as fat as a function of frequency [15–18].

Measurements of 30 different tissue types by Gabriel [15–18] indicate that the relative dielectric permittivity and conductivity, of high-water-content tissues (such

as muscle or malignant tumors) are about an order of magnitude greater than those of low-water-content tissues (such as fat or normal breast tissue). As illustrated in Fig 1.5, this contrast between high- and low-water-content tissues persists over the entire radio-frequency (RF) spectrum from power frequencies through millimeter waves.

In the study performed by Li et al. [12] is verified that the previous experimental data (Chaudhary et al., Surowiec et al., Joines et al. [19–21]) are in accordance with differential equation formulation for a first-order dispersion (Debye Model):

$$\varepsilon_r = \varepsilon_\infty + \frac{\Delta\varepsilon}{1 + j2\pi\nu\tau} - j\frac{\sigma}{2\pi\nu\varepsilon_0} \tag{1.5}$$

where $\Delta\varepsilon = \varepsilon_s - \varepsilon_\infty$, ε_∞ is the permittivity at frequencies $j2\pi\nu\tau >> 1$, ϵ_s the permittivity at $j2\pi\nu\tau << 1$ and τ is the time constant of the relaxation mechanism in the tissue, see Fig. 1.6.

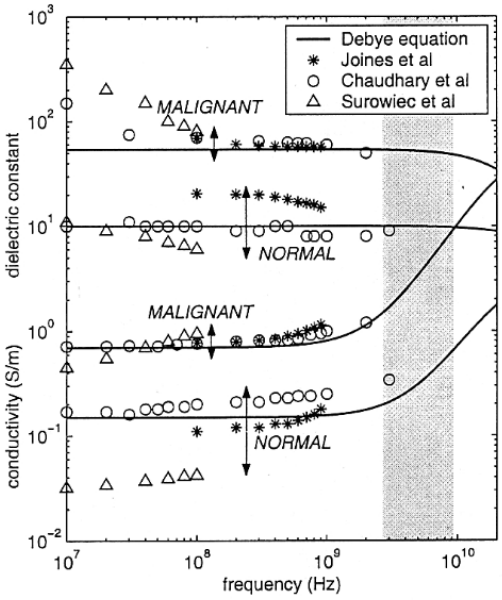

Figure 1.6: Single-pole Debye curve fits of measured baseline dielectric-properties data for normal and malignant breast tissue at radio and microwave frequencies [12].

The Debye parameters have been chosen to fit the published data for normal and tumor breast tissue are, respectively:

$$\begin{aligned} \varepsilon_\infty &= 7,\ \Delta\varepsilon = 3,\ \sigma = 0.15,\ \tau = 6.4 \\ \varepsilon_\infty &= 4,\ \Delta\varepsilon = 46,\ \sigma = 0.70,\ \tau = 6.4. \end{aligned} \tag{1.6}$$

To preserve the heterogeneity of normal breast tissue, the Debye parameters have a variation of 20% around an estimated baseline. This variation represents an upper bound on reported breast tissue variability, which presumably covers the range from fat (smallest values) to fibroglandular tissue (largest values). The conclusion from these measurements is a significant contrast between malignant tissues and normal breast tissues, approximately 4:1 in permittivity and between 4-8:1 in conductivity along the frequency band of microwaves [11–13].

1.3.2 A complex problem

The estimate of breast dielectric properties is a crucial point for the outcome of an accurate cancer detection methodology. This estimate represents a complex problem due the heterogeneity of human breast. The heterogeneity of the breast is expressed in terms of the intra-class variability (breast tissue composition) and inter class-variability (different tissue composition between different breasts).

In recent large scale study performed by Lazebnik et al.[22], the dielectric properties of a large number of normal breast tissue samples obtained from breast reduction surgeries at the University of Wisconsin and University of Calgary hospitals were experimentally characterized in the wideband microwave-frequency. The dielectric spectroscopy measurements were conducted from 0.5 to 20 GHz using a precision open-ended coaxial probe. The tissue composition within the probe's sensing region was quantified in terms of percentages of adipose, fibroconnective and glandular tissues. The study of distributions of sample tissue compositions demonstrates that the dielectric properties of breast tissue are primarily determined by the adipose content of each tissue sample. The second result is that secondary factors such as patient age, tissue temperature and time between excision and measurement have only negligible effects on the observed dielectric properties.

Finally, the main conclusion of this study is that dielectric properties of normal breast tissue across the microwave frequency range is larger than suggested by most of the earlier small-scale studies, and that the dielectric properties of some types of normal breast tissues are much higher than previously reported, Fig. 1.7.

In a second large scale study, Lazebnik et al.[23], with same techniques, experimentally characterized the dielectric properties of malignant tissue in the wideband microwave-frequency. In contrast with normal tissue, the dielectric properties of malignant tissues are high and span a relatively small range.

Moreover, Lazebnik et al. found the dielectric properties for the group: low adipose tissue content (0-30%), median adipose (31-84%), high adipose (85-100%), and cancer tissue. Dielectric constant and effective conductivity dispersion curves, Figure 1.7, are obtained for each group by fitting the data with single pole Cole-Cole models:

$$\varepsilon_r = \varepsilon_\infty + \frac{\Delta\varepsilon}{1 + (j2\pi\nu\tau)^{1-\alpha}} + j\frac{\sigma}{2\pi\nu\varepsilon_0} \tag{1.7}$$

where $\Delta\varepsilon = \epsilon_s - \varepsilon_\infty$ and α is the Cole-Cole model parameter which is estimated from the experimental data.

Table 1.1: Mean Cole-Cole parameters for the dielectric properties of the three adipose-defined groups and cancer group.

	ε_∞	$\Delta\varepsilon$	τ(ps)	σ(S/m)	α
low adipose	7.2	46.0	10.3	0.80	0.05
median adipose	6.1	19.3	11.5	0.30	0.06
high adipose	3.6	3.3	15.2	0.05	0.05
cancer	6.7	50.1	10.5	0.80	0.05

In Table 1.1 are shown the mean Cole-Cole model parameter for the group: low adipose tissue content (0-30%), median adipose (31-84%), high adipose (85-100%),

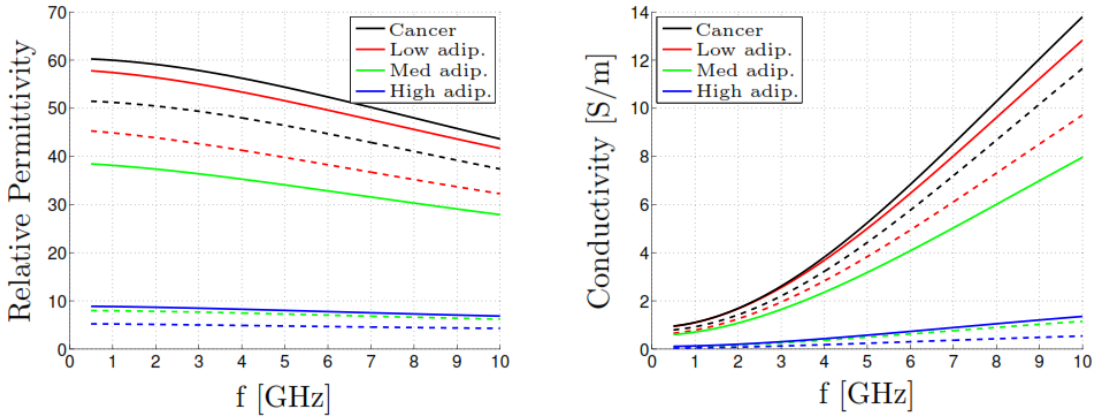

Figure 1.7: Permittivity and conductivity values from the University of Wisconsin, Madison study [23]. The data represents the values for cancerous tissue (black line) and normal tissue obtained from cancer surgeries with low, medium and high content of adipose tissue (red, green, and blue lines, respectively). For each tissue type, the data for the 25 percentile is given by the dashed line and the data for the 75 percentile by the solid line.

and cancer tissue, used in data fitting. The results of analysis indicate that the microwave frequency dielectric properties contrast between malignant breast tissues and normal adipose dominated breast tissues is large, ranging up to a 10:1 contrast when considering almost entirely adipose breast tissue as the reference. However, the dielectric properties contrast between malignant and normal fibroconnective-glandular breast tissues is considerably lower, no more than approximately 10%.

Chapter 2

Reconstruction Algorithm

Microwave imaging is a technique aimed at sensing a given scene by means of interrogating microwaves. This active technique considered for a long time an emerging technique has recently proved capable of providing excellent diagnostic capabilities in several areas. To localize, shape, and reconstruct an unknown target located in an investigation domain and surrounded by measurement probes able to acquire the samples of the scattered field, several different approaches can be applied. Those considered in this thesis are inverse scattering - based procedures, which address the data inversion in several different ways depending on the target itself (e.g., strongly or weakly contrasted bodies, conducting objects) or on the imaging configuration and operation conditions. Inverse scattering is an ill-posed problem, the solution of this problem is found through Time-Reversal Imaging (TR), then scatterer is localized by MUltiple SIgnal Classification algorithm (MUSIC)[24]. This method, called TR-MUSIC, is developed by Devaney [25–27].

In this thesis a Multi-frequency approach is considered: data collected at different frequencies are employed to improve the performance of the single-frequency case, then, they are combined in Geometrical Mean MUSIC (GM-MUSIC).

2.1 Physical Principles

When an object, which in this context is also called target or scatterer, is present in the propagation medium, the wave produced by the source interacts with it and the field distribution is affected by the presence of the scatterer.

The situation is schematized in Figure 1.4 , which describes a scattering configuration involving only dielectrics or materials with a finite electric conductivity. In this context, let us assume a non-magnetic object to be characterized by permittivity ε and conductivity σ, immersed in a homogeneous and infinite medium (free - space scattering) with ε_b and σ_b.

The perturbed field (which is the only field that can be measured in the presence of the object) is indicated by E_{tot}. This field is clearly different from the field generated by the source when the object in not present, which is indicated as incident or unperturbed field and denoted by E_{inc}. The incident field is a known quantity if the source is completely characterized. Moreover, we can write:

$$E_{tot}(\boldsymbol{r}) = E_{inc}(\boldsymbol{r}) + E_{sc}(\boldsymbol{r}) \tag{2.1}$$

where $\boldsymbol{r}$ denotes position vector, $E_{sc}(\boldsymbol{r})$ denotes the scattered field and represents the interaction between the incident field and the target.

Two situations usually occur. In the first one, the object is completely known and one has to compute the perturbed fields. This is called *direct scattering problem.* For the free - space configuration in Figure 1.4 , the following quantities are assumed as known quantities in the direct scattering problem: $E_{inc}(\boldsymbol{r}),\ \forall\ \boldsymbol{r} \in \mathbb{R}$, ε_b and σ_b, the space region V_0 occupied by the object and the dielectric parameters of the target, ε and σ. The goal is the computation of the scattered fields $E_{sc}(\boldsymbol{r})$ everywhere.

In the second situation considered, which is of paramount importance for this thesis, the object is unknown and one has to deduce information on it from some measurements of the perturbed field generally collected outside the object. This is called an *inverse scattering problem.* For the free - space configuration considered, in the inverse scattering problem, the following quantities are still assumed known: $E_{inc}(\boldsymbol{r}),\ \forall\ \boldsymbol{r} \in \mathbb{R}$, ε_b and σ_b. Moreover, it is assumed that the total electric field $E(\boldsymbol{r})$ is known quantity (e.g., obtained by suitable measurements) only for $\boldsymbol{r} \notin V_0$. On the contrary, V_0, ε and σ are unknown quantities, and these ones are the objective of the computation. It is evident that in practice it is impossible to measure $E(\boldsymbol{r}),\ \forall\ \boldsymbol{r} \notin V_0$, and so these vectors are usually available at a discrete set of points.

2.2 Inverse Scattering Problem

In order to describe scattering problems, it is necessary to deduce equations relating the measured values of the electromagnetic field to the properties of the scatterer under test.

We consider the mathematical model in which wave propagation is governed in a inhomogeneous medium by the Helmholtz equation:

$$(\nabla^2 + k^2)E(\boldsymbol{r}) = f(\boldsymbol{r}) \tag{2.2}$$

where $f : \mathbb{R}^n \to \mathbb{C}$ is a given function with compact support and k is the wavenumber. This equation can be expressed in terms of radiation integral as:

$$E(\boldsymbol{r}) = \int_{\mathbb{R}^n} f(\boldsymbol{R})G(\boldsymbol{r}, \boldsymbol{R})d\boldsymbol{R} \tag{2.3}$$

where $\boldsymbol{R}$ is the observation point, and $G(\boldsymbol{r}, \boldsymbol{R})$ is the free-space Green's function (see Appendix A). Notice that Green's tensor is related to the radiation produced by an elementary source and provides a solution to the following tensor equation:

$$(\nabla^2 + k^2)G(\boldsymbol{r}, \boldsymbol{R}) = I\delta(\boldsymbol{r} - \boldsymbol{R}) \tag{2.4}$$

where I is identity tensor and $\delta(\boldsymbol{r}-\boldsymbol{R})$ denotes Dirac delta function. The expression for the Green's function depends on the dimension of the space, for two-dimensional space is [28]:

$$G(\boldsymbol{r}, \boldsymbol{R}) = -\frac{i}{4}h_0^{(2)}(k|\boldsymbol{r} - \boldsymbol{R}|) \tag{2.5}$$

where $|\cdot|$ represents Euclidean distance, $h_0^{(2)}$ is the Hankel function with order=0 and kind=2, (Appendix B).

Let us consider the presence of a scatterer, then substituting equation (2.3) (with $E(\boldsymbol{r}) = E_{sc}(\boldsymbol{r})$) into (2.1) we have:

$$E_{tot}(\boldsymbol{r}) = E_{inc}(\boldsymbol{r}) + \int_{\mathbb{R}^n} \tau(\boldsymbol{R}) E(\boldsymbol{R}) G(\boldsymbol{r}, \boldsymbol{R}) d\boldsymbol{R} \tag{2.6}$$

where $\tau(\boldsymbol{R})$ is the scattering amplitude.

Over the last two decades, significant research activities were focused on solution of inverse scattering problem for breast cancer detection. The resolution method can be grouped into two categories: one which aims at reconstructing the dielectric and conductivity maps of the breast, *non-linear inverse scattering method*, and another which detects and localizes in-homogeneities in the breast *linear inverse scattering method*.

2.2.1 Non-Linear Inverse scattering

In nonlinear inverse scattering, the measured field is used as input to an inverse problem with a forward problem based on Maxwell's equations. This forward problem is nonlinear in terms of the unknown constitutive parameters and solving the inverse problem is thus a non-trivial matter. The method was introduced for imaging of the breast by Meaney et al. [29] in 1995 and other significant work was performed by Souvorov et al. [30] in 1998. The nonlinear inverse problem is solved using an algorithm based on the iterative Newton scheme or a method derived from this. In these algorithms, the distribution of constitutive parameters in the imaging domain is updated in steps. In each iteration, the scattered field from the current parameter distribution is calculated and compared with the measured field. The update of the distribution may then be found by linearizing the nonlinear inverse problem. A number of different implementations of the Newton algorithm have been reported, such as the Gauss-Newton algorithm [29], Newton-Kantorovic [30], the inexact Newton algorithm [31] and the conjugate gradient algorithm with line search [32]. These techniques require that the scattered field is calculated in each iteration using a forward solver, e.g., based on finite-difference time-domain (FDTD), the finite-element method (FEM) or the methods of moments (MoM). Such forward solvers are computationally expensive and this is most likely the reason why the nonlinear imaging algorithms are not as widely applied as the computationally less expensive linear algorithms.

2.2.2 Linear Inverse scattering

The second class of breast imaging methods are those that are based on linear scattering models. In this case, mutual scattering between the different part of the breast are neglected (in the model) and the imaging problems just consists of a linear inversion. Of course, as simplified models are employed, only "qualitative" information can be gathered and, hence, a further classification step is generally needed. However, problems of reliability and computational burden are avoided.

The imaging algorithm most frequently applied in linear method is the confocal or delay-and-sum imaging algorithm [11], a technique which has been used in synthetic aperture radar for many years. When this algorithm is used, a short pulse is transmitted and the response in time is measured at the receiving antennas. The interior of the breast is then divided into a number of pixels and the resulting image is created by adding the measured signals delayed by the travel time for the pulse from the transmitting antenna to the individual pixels and back to the receiver. If a scatterer is present at a pixel, the sum of the delayed signals will be at a maximum. This type of algorithm assumes that the scattering effects are due to point scatterers and that the scattered fields from the individual point scatterers do not interact with other scatterers in the imaging domain. Hence, the imaging problem is solved as a linear inverse problem.

An accurate estimate of the travel time from the antennas to each pixel in the imaging domain is a necessity for using the confocal imaging algorithm. This implies that the constitutive parameters of the healthy tissue must be known in advance which may pose a problem, given the large variations in tissue properties described above. In addition to this, the confocal imaging algorithm seems to have difficulties in dealing with differences in the background constitutive parameters, i.e., it is required that the coupling liquid is closely matched to the breast tissue of the patient.

In recent years, Time-Reversal method (TR) has emerged as a technique microwave imaging of the breast. Time Reversal methods are based on the time-reversibility of the wave equation in a lossless medium. Accordingly, images are obtained by retransmitting the received signals after they are time reversed. This allows to obtain focusing on the more strongly scattering objects. It has been shows that this method exhibits good stability response against background uncertainties specially if losses are suitably compensated for [33].

In this thesis we focus in detection and localization of breast lesions. We use a linear scattering method based on Time-Reversal method and Multiple Signal Classification (MUSIC) [24], it is developed by Devaney [25–27] and is called TR-MUSIC .

2.3 Time Reversal-MUSIC

Let us rewrite the inverse scattering equation:

$$E(\boldsymbol{r})_t ot = E_{inc}(\boldsymbol{r}) + \int_{\mathbb{R}^n} \tau(\boldsymbol{R}) E(\boldsymbol{R}) G(\boldsymbol{r}, \boldsymbol{R}) d\boldsymbol{R} \tag{2.7}$$

assuming as known the value of E_{inc}, we want to find a solution of the integral equation in discrete frequency domain.

2.3.1 Time Reversal Imaging

Consider an array of N antennas, centered at the space point $\boldsymbol{R}_1, ..., \boldsymbol{R}_N$. Each antenna is assumed to radiate a field E in a domain D in which are embedded one or

more scatterers (targets). We make the simplifying assumptions that the antennas are monopoles (ideal point sources) and the targets are ideal point scatterers and, in addition, neglect all multiple scattering between targets. Under these assumptions the wavefield radiated by j-th antenna element and the resulting scattered field are equal to:

$$E_{inc,j}(\boldsymbol{r},\omega) = G(\boldsymbol{r},\boldsymbol{R}_j,\omega)e_j(\omega) \tag{2.8}$$

$$E_{sc,j}(\boldsymbol{r},\omega) = \sum_{m=1}^{M} G(\boldsymbol{r},\boldsymbol{X}_m,\omega)\tau_m(\omega)G(\boldsymbol{X}_m,\boldsymbol{R}_j,\omega)e_j(\omega) \tag{2.9}$$

where $\omega = 2\pi\nu$ is the angular frequency, $\boldsymbol{X}_m$ is m-th scatter location and $e_j(\omega)$ is input voltage applied at the j-th terminals of antenna. When all antennas are simultaneously excited using the voltage $e_j(\omega)$, the total incident and scattered fields are:

$$E_{inc}(\boldsymbol{r},\omega) = \sum_{j=1}^{N} E_{inc,j}(\boldsymbol{r},\omega) = \sum_{j=1}^{N} G(\boldsymbol{r},\boldsymbol{R}_j,\omega)e_j(\omega) \tag{2.10}$$

$$E_{sc}(\boldsymbol{r},\omega) = \sum_{j=1}^{N} E_{sc,j}(\boldsymbol{r},\omega) = \sum_{j=1}^{N}\sum_{m=1}^{M} G(\boldsymbol{r},\boldsymbol{X}_m,\omega)\tau_m(\omega)G(\boldsymbol{X}_m,\boldsymbol{R}_j,\omega)e_j(\omega) \tag{2.11}$$

The voltage output v_l collect at the l-th antenna is assumed to be equal to the amplitude of scatterer field as measured at l-th antenna:

$$v_l(\omega) = \sum_{j=1}^{N} E_{sc,j}(\boldsymbol{R}_l,\omega) = \sum_{j=1}^{N}\sum_{m=1}^{M} G(\boldsymbol{R}_l,\boldsymbol{X}_m,\omega)\tau_m(\omega)G(\boldsymbol{X}_m,\boldsymbol{R}_j,\omega)e_j(\omega) \tag{2.12}$$

introducing the N-dim Green function vector $\boldsymbol{G}_m(\omega)$:

$$\boldsymbol{G}_m(\omega) = [\boldsymbol{G}_m(\boldsymbol{R}_1,\boldsymbol{X}_m,\omega),\ldots,\boldsymbol{G}_m(\boldsymbol{R}_N,\boldsymbol{X}_m,\omega)]^T \tag{2.13}$$

and defining:

$$\boldsymbol{A}(\omega) = \sum_{m=1}^{M} \tau_m(\omega)\boldsymbol{G}_m(\omega)\boldsymbol{G}_m^T(\omega) \tag{2.14}$$

we can express (2.12) in compact matrix notation:

$$v_l(\omega) = \boldsymbol{A}(\omega)\boldsymbol{e}(\omega) \tag{2.15}$$

where $\boldsymbol{A}(\omega)$ is called *Multistatic Response Matrix* (MSR) and represents the matrix propagator. Notes that $\boldsymbol{e}(\omega) = [e_1(\omega),\ldots,e_N(\omega)]$ is the input voltage vector. The correlation matrix, called *Time Reversal Matrix* (TRM) [25–27], is constructed as follows:

$$\boldsymbol{T}(\omega) = \boldsymbol{A}^H(\omega)\boldsymbol{A}(\omega) = \boldsymbol{A}^*(\omega)\boldsymbol{A}(\omega) \tag{2.16}$$

where $\boldsymbol{A}^H(\omega)$ and $\boldsymbol{A}^*(\omega)$ are the Hermitian and the complex conjugate of $\boldsymbol{A}(\omega)$, respectively. The second equality in (2.16) follows from the fact that MSR in

symmetric, so $\boldsymbol{A}^H = \boldsymbol{A}^*$. In terms of green function vectors we conclude using (2.14) that:

$$\begin{aligned}\boldsymbol{T}(\omega) &= \left[\sum_{m=1}^{M} \boldsymbol{\tau}_m(\omega)\boldsymbol{G}_m(\omega)\boldsymbol{G}_m^T(\omega)\right]^* \cdot \left[\sum_{m'=1}^{M} \boldsymbol{\tau}_{m'}(\omega)\boldsymbol{G}_{m'}(\omega)\boldsymbol{G}_{m'}^T(\omega)\right] \\ &= \sum_{m=1}^{M}\sum_{m'=1}^{M} \Lambda_{m,m'}\boldsymbol{G}_m^*(\omega)\boldsymbol{G}_{m'}^T(\omega)\end{aligned} \tag{2.17}$$

where

$$\Lambda_{m,m'} = \boldsymbol{\tau}_m^* \tau_{m'} \left\langle\ \boldsymbol{G}_m(\omega), \boldsymbol{G}_{m'}(\omega)\ \right\rangle \tag{2.18}$$

and angular brackets $\langle\ \cdot\ ,\ \cdot\ \rangle$ stand for inner product in $\mathcal{C}^N$.

The time-reversal matrix $\boldsymbol{T}(\omega)$ is Hermitian and non-negative. Because of these facts the matrix possesses a complete set of orthonormal eigenvectors having non-negative eigenvalues. If $M \leq N$, the rank of $\boldsymbol{T}(\omega)$ will be equal to M, so that there are M non-zero eigenvalues.

2.3.2 MUSIC Algorithm

The term MUltiple SIgnal Classification (MUSIC) is used to describe experimental and theoretical techniques involved in determining the parameters of multiple wave-fronts arriving at an antenna array from measurements made on the signals received at the array elements, by reference Schmidt [24]. The general problem considers antennas with arbitrary locations and arbitrary directional characteristics (gain, phase, polarization) in a noise interference environment of arbitrary covariance matrix . The MUSIC algorithm makes use of the fact that the time-reversal matrix $\boldsymbol{T}(\omega)$ is a projection operator onto the subspace of $\mathcal{C}^N$ spanned by the Green function vectors (*signal subspace*, $\mathcal{S}$) and that the *noise subspace* $\mathcal{N}$ is spanned by the eigenvectors of $\boldsymbol{T}(\omega)$ having zero eigenvalue, i.e.

$$\left\langle\ \boldsymbol{G}_m^*(\omega), \boldsymbol{V}_{m_0}(\omega)\ \right\rangle = \left\langle\ \boldsymbol{G}_m(\omega), \boldsymbol{V}_{m_0}^*(\omega)\ \right\rangle = 0 \tag{2.19}$$

where $\boldsymbol{V}_{m_0}(\omega)$ for $m_0 = M+1, ..., N$ are the eigenvectors of $\boldsymbol{T}(\omega)$ having zero eigenvalues. Defying the *steering matrix* $\boldsymbol{A}_k(\omega)$ as the MSR-matrix in the trial points $\boldsymbol{r}_k$ of domain D:

$$\boldsymbol{A}_k(\omega) = \boldsymbol{G}_k(\omega)\tau_m(\omega)\boldsymbol{G}_k(\omega)^T. \tag{2.20}$$

where $\boldsymbol{G}_k(\omega) = [\boldsymbol{G}(\boldsymbol{R}_1, \boldsymbol{r}_k, \omega), \ldots, \boldsymbol{G}(\boldsymbol{R}_N, \boldsymbol{r}_k, \omega)]$ and we can formulate the *pseudospectrum* expression:

$$\Phi(\boldsymbol{r}_k, \omega) = \frac{1}{|P[\boldsymbol{A}_k(\omega)]|^2} = \frac{1}{\left|\displaystyle\sum_{m_0=M+1}^{N} \left\langle\ \boldsymbol{A}_k(\omega), \boldsymbol{V}_{m_0}^*(\omega)\ \right\rangle\right|^2} \tag{2.21}$$

where $P[\ \cdot\ ]$ is projection operator in $\mathcal{N}$. The crucial point concerning eq. (2.21) is that the scatterers are identified by the peaks in the Pseudospectrum in deterministic way.

2.3.3 MUSIC in monostatic configuration

The acquisition system considered so far is an array of N antennas positioned equidistant along a circumference, in which: one antenna transmits and receives the signal from $\boldsymbol{R}_l$ position, the other N-1 antennas receive only. This operation is repeated N times, one for each antenna. This configuration of antennas is called *multistatic configuration*, Fig. 2.1a.

In this thesis we consider a different system configuration: the *monostatic configuration*, Fig. 2.1b. In monostatic configuration only one antenna transmits and receives from the position $\boldsymbol{R}_l$. After the measure, the antenna is moved in an other position and the measure is rerun. The N positions $\boldsymbol{R}_1, \ldots, \boldsymbol{R}_N$ occupied by the antenna are equally spaced along a circumference.

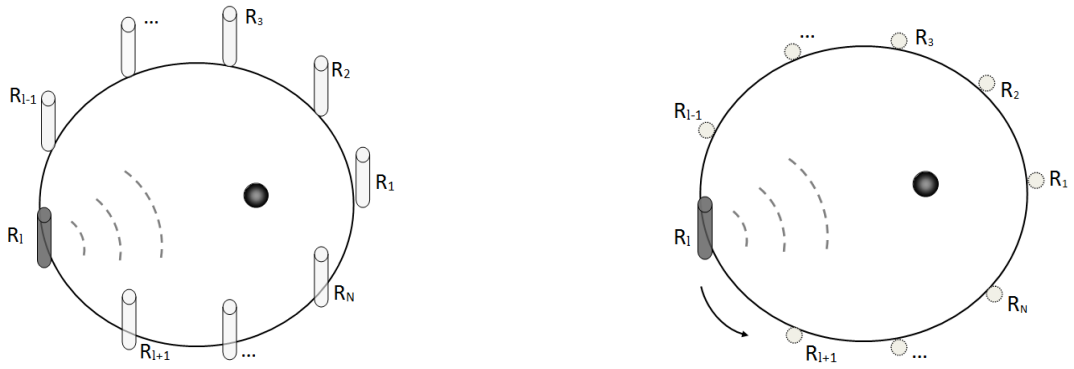

(a) Multistatic configuration **(b)** Monostatic configurartion

Figure 2.1: (a)Multistatic configuration: the antenna in R_l transmits and receive the signal, the other N antennas receive only. (b) Monostatic configuration: one antenna in R_l transmits and receive the signal.

In this system configuration, the voltage output from l-th antenna position writes as:

$$v_l(\omega) = E_{sc,l}(\boldsymbol{R}_l, \omega) = \sum_{m=1}^{M} G(\boldsymbol{R}_l, \boldsymbol{X}_m, \omega)\tau_m(\omega)G(\boldsymbol{X}_m, \boldsymbol{R}_l, \omega)e(\omega) = A_l(\omega)e(\omega) \tag{2.22}$$

We can define the vector of voltage output from the N antenna positions as:

$$\boldsymbol{v}(\omega) = [v_1, v_2, \ldots, v_N]^T \tag{2.23}$$

and in terms of Monostatic Response vector (MoSR), we can write:

$$\boldsymbol{v}(\omega) = \boldsymbol{A}(\omega)e(\omega). \tag{2.24}$$

where $\boldsymbol{A}(\omega) = [A_1(\omega), A_2(\omega), \ldots, A_N(\omega)]^T$. Achievable performance of MUSIC can be equivalently and more conveniently studied by employing the projector over the signal subspace $\mathcal{S}$:

$$|P[\boldsymbol{A}_k(\omega)]|^2 = |(I - Q)[\boldsymbol{A}_k(\omega)]|^2 \tag{2.25}$$

where $Q[\ \cdot\ ]$ is projection operator in $\mathcal{S}$ [34] and $\boldsymbol{A}_k(\omega)$ is the *steering vector*, defined as the MoSR-vector in the trial points $\boldsymbol{r}_k$ of domain D:

$$\boldsymbol{A}_k(\omega) = [A_{k1}, A_{k2}, \ldots, A_{kN}] \tag{2.26}$$

where $A_{kl} = G(\boldsymbol{R}_l, \boldsymbol{r}_k, \omega)\tau G(\boldsymbol{r}_k, \boldsymbol{R}_l, \omega)$. From the equations (2.24) it is clear that the computation of $\boldsymbol{T}(\omega)$ is not necessary since:

$$|(I - Q)[\boldsymbol{A}_k(\omega)]|^2 = 1 - |\langle \boldsymbol{A}(\omega), \boldsymbol{A}_k(\omega)\rangle|^2. \tag{2.27}$$

from that:

$$\Phi(\boldsymbol{r}_k, \omega) = \frac{1}{1 - |\langle \boldsymbol{A}_k(\omega), \boldsymbol{A}(\omega)\rangle|^2} \tag{2.28}$$

2.3.4 GM-MUSIC Algorithm

In this thesis a multi-frequency approach is considered, data are collected at different frequencies and are combined to improve the performance of the single-frequency case. In Ruvio et al. [34–37], two multi-frequency method are proposed:

Wide-band MUSIC algorithm (WB-MUSIC):

$$\Phi_{WB}(\boldsymbol{r}_k) = \frac{1}{\sum_{i=1}^{N_\nu} \left| P_i[\boldsymbol{A}_k(\omega_i)] \right|^2} \tag{2.29}$$

Interferometric MUSIC algorithm (I-MUSIC):

$$\Phi_I(\boldsymbol{r}_k) = \frac{1}{\prod_{i=1}^{N_\nu} \left| P_i[\boldsymbol{A}_k(\omega_i)] \right|^2} \tag{2.30}$$

where N_ν is the number of frequency. Here, we propose a multifrequency approach algorithm defined as the geometric mean of single frequency pseudospectra:

$$\Phi_{GM}(\boldsymbol{r}_k) = \sqrt[N_\nu]{\prod_{i=1}^{N_\nu} \Phi_i(\boldsymbol{r}_k, \omega_i)} \tag{2.31}$$

Our multi-frequency formulation allows a better interpretation of data, as well as a correct error estimation, it called Geometrical Mean MUSIC (GM-MUSIC).

2.4 Reconstruction Process

In order to achieve images of the breast under test different processing steps are required, these steps basically consists in:

- clutter cancellation/mitigation;
- preliminary assessment of scattering scenario;
- reconstruction algorithm (discussed in § 2.3);
- evaluation of the reconstruction.

This section discusses the operations of pre and post processing, these steps and reconstruction algorithm accomplish our microwave imaging algorithm.

2.4.1 Clutter Cancellation

Clutter mitigation basically aims at canceling all those unwanted contributions that are not useful in the reconstruction stage. Clutter arises due to the reflection from internal antenna reverberations and from the skin layer. These artefacts are typically several orders of magnitude greater than the contribution coming from the tumor and tend to mask the latter while imaging.

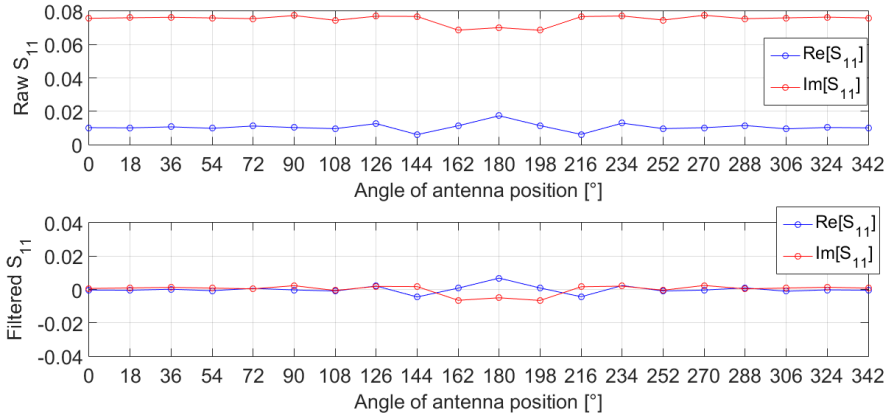

Figure 2.2: S_{11} raw signal, top graph, and filtered signal with average trace subtraction, bottom graph. Blue line: real part of the signal and red line: imaginary part.

Considering the S_{11} signal, defined as:

$$S_{11} = \left.\frac{b_1}{a_1}\right|_{a_2=0} \tag{2.32}$$

where a_j is the incident wave and b_i the reflected one, see § 4.1.3. The elimination of the non-useful contribution is made by subtracting the average component from the signal S_{11}, this consists in filtering out low frequency content (with respect to the antenna's location spatial variable). The zero-mean signal enhances the variations produced by the target scattering, see Fig. 2.2.

2.4.2 Assessment of scattering scenario

Preliminary assessment of scattering scenario basically means to try to estimate some breast features that can be useful in the reconstruction stage. That is, the average dielectric and conducting breast properties that can be used to reduce blurring in the detection procedure. For this purpose, we have analyzed a number of MRI-derived breast phantoms for breast cancer detection and treatment applications, download from the UWCEM Numerical Breast Phantom Repository [38]. The numerical phantoms are classified according to their radiographic density, defined by the American College of Radiology [39], as follows: ACR Class 1 - *Mostly Fatty* (<25% glandular tissue), ACR Class 2 - *Scattered Fibroglandular*(25-50% glandular), ACR Class 3 - *Hetergeneously Dense* (51-75% glandular), ACR Class 4 - *Very Dense*(>75% glandular), Fig. 2.3. Each phantom is comprised of a 3D grid

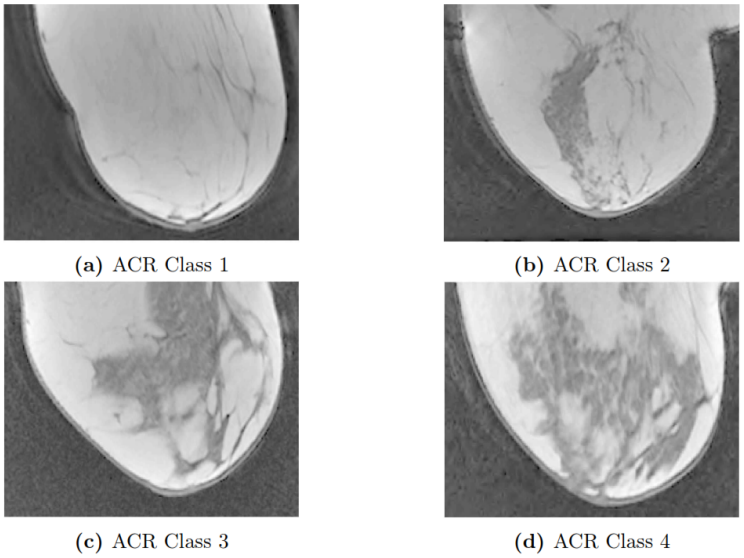

(a) ACR Class 1 **(b)** ACR Class 2

(c) ACR Class 3 **(d)** ACR Class 4

Figure 2.3: Sagittal slice from a 3D breast MRI phantoms: (a) ACR Class 1 - Mostly Fatty, (b) ACR Class 2 - Scattered Fibroglandular, (c) ACR Class 3 - Heterogeneously Dense, (d) ACR Class4 - Very Dense. UWCEM Numerical Breast Phantom Repository [38].

of cubic voxels, where each voxel (0.5mm x 0.5mm x 0.5mm) contains informations on the tissue type and its electrical properties (Debye parameters, see § 1.3.1).

The goal is to estimate a mean value for the Debye parameters (ε_∞, $\Delta\varepsilon$, σ and τ is set at 13ps) and a variability range which represents the breast classes variability. In Figures 2.4a, 2.4b, 2.4c and 2.4d are shown the Debye parameter distribution for each breast class. The histograms show a bimodal distribution: the first mode represents the adipose tissue, the second one fibroglandular tissue. We chose the adipose tissue as average breast tissue, because the element numerosity of the adipose tissue mode is two orders of magnitude greater than the fibroglandular one. The amount of elements in the adipose mode is about 80%. For the adipose mode, we compute the mean values and standard deviations of each Debye parameter, Tab. 2.1. The total mean values and the total standard deviations of each Debye

Table 2.1: Mean value $\overline{x}_i$ and standard deviation $\sigma_{x,i}$ of Debye parameter distributions for each phantom classes. w_i it the weight of adipose tissue.

		ε_∞		$\Delta\varepsilon$		σ(S/m)	
	w_i	$\overline{x}_i$	$\sigma_{x,i}$	$\overline{x}_i$	$\sigma_{x,i}$	$\overline{x}_i$	$\sigma_{x,i}$
ACR1	0.8	3.2	0.2	1.7	0.5	0.05	0.02
ACR2	0.6	3.2	0.3	1.8	0.7	0.05	0.02
ACR3	0.3	4	2	4	1	0.08	0.05
ACR4	0.2	4	2	4	2	0.10	0.08

parameter are computed weighing the values on adipose tissue percentage in the

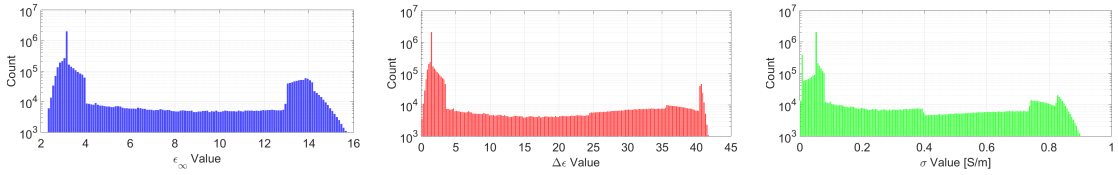

(a) ACR Class 1.

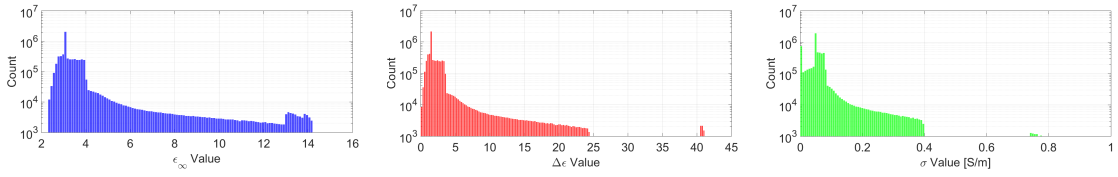

(b) ACR Class 2.

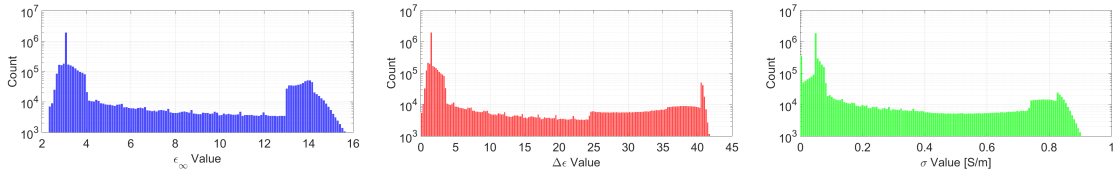

(c) ACR Class 3.

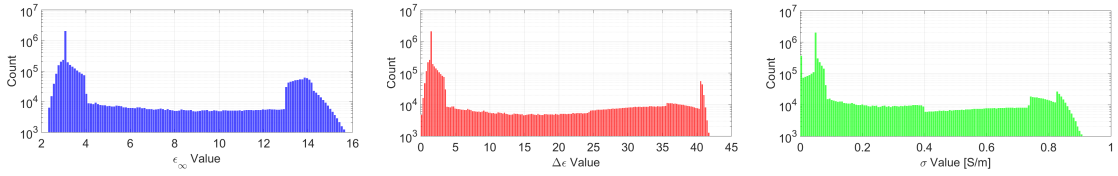

(d) ACR Class 4.

Figure 2.4: The Histogram distribution of Debye parameters for each phantom classes: ε_∞-distribution (blue colour), $\Delta\varepsilon$-distribution (red colour) and σ-distribution (green colour).

class, as:

$$\overline{x} = \frac{\sum_{i=1}^{N_c} \overline{x}_i \cdot w_i}{\sum_{i=1}^{N_c} w_i} \qquad \sigma_x = \frac{\sqrt{\sum_{i=1}^{N_c} (w_i \cdot \sigma_{x,i})^2}}{\sum_{i=1}^{N_c} w_i} \tag{2.33}$$

where $N_c = 4$ is the number of phantom classes. The values in Tab. 2.2 represent the electrical parameters of the average breast.

Table 2.2: Mean value $\overline{x}$ and standard deviation σ_x of Debye parameters for the average adipose tissue.

ε_∞		$\Delta\varepsilon$		σ(S/m)	
$\overline{x}$	σ_x	$\overline{x}$	σ_x	$\overline{x}$	σ_x
3.2	0.6	1.9	0.8	0.05	0.04

2.4.3 Evaluation of the reconstruction

After locating the target through MUSIC algorithm, it is necessary to characterize the goodness of the reconstruction, thus some features are computed:

- *Spatial features:* Full Width at Half Maximum (FWHM), Spatial Displacement(SD) and p-value, that give a measure of resolution and spatial delocalization between target and reconstructed point;
- *Contrast features:* Signal-to-Clutter Ratio (SCR) and Signal-to-Clutter Mean Ratio (SCMR), that give a measure of contrast between signal and background.

Spatial Features

MUSIC Algorithm identifies the target position in the maximum of pseudospectrum. Theoretically the reconstructed target is represented by a Dirac delta function of infinite value, but in real reconstruction it takes the form of a spread curve with a finite maximum. In many circumstances, the reconstructed target is not symmetrical with respect to its maximum, thus we choose the centroid of the curve at Half Maximum (HM) as estimation of target position.

Consider the Figure 2.5, the point target located in $X(x, y)$ and the 2-D spread curve cut at HM and centered in $C(x, y)$ are summarized. The computation of the spatial metric is performed in the maximum variance configuration obtained through the PCA (Principal Component Analysis) method. PCA is mathematically defined as an orthogonal linear transformation that transforms the data to a new coordinate system such that the greatest variance by some projection of the data comes to lie on the first coordinate (called the first principal component), the second greatest variance on the second coordinate, and so on [40]. In the considered 2D problem, the new coordinate system (ρ, ϕ), defined by PCA, describes

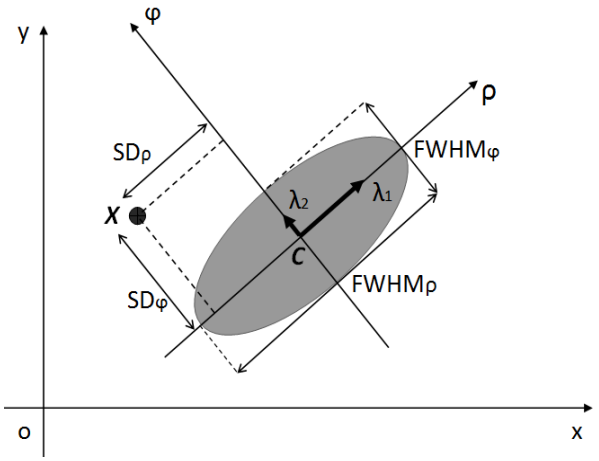

Figure 2.5: Target $X(x, y)$ and Centroid $C(x, y)$ in PCA coordinate system.

radial and angular measures respectively. We define the target spread in terms of Full Width at Half Maximum (FWHM) as:

$$FWHM_{\rho,\phi} = 2\alpha\sqrt{\lambda_{1,2}} \tag{2.34}$$

where $\lambda_{1,2}$ are the eigenvalues of PCA and $\alpha = 1.96$ represents the 95% confidence interval. We define Spatial Displacement as the distance between target and centroid, i.e.:

$$SD_{\rho,\phi} = X_{\rho,\phi} - C_{\rho,\phi} \tag{2.35}$$

where $X_{\rho,\phi}$ and $C_{\rho,\phi}$ are target position and centroid in PCA coordinate system. The last spatial feature is the p-value, which represents a significance level of obtaining a correct reconstruction:

$$p - value_{\rho,\phi} = 2 \cdot (1 - F[X_{\rho,\phi}, C_{\rho,\phi}, \sigma_{\rho,\phi}]) \tag{2.36}$$

where $F[X, C, \sigma]$ is the cumulative function, defined as:

$$F[X, C, \sigma] = \frac{1}{\sigma\sqrt{2\pi}} \int_{-\infty}^{X} e^{-\frac{(t-C)^2}{2\sigma^2}} dt \tag{2.37}$$

and σ is the standard deviation, defined as:

$$\sigma_{\rho,\phi} = \frac{FWHM_{\rho,\phi}}{2\sqrt{2 \cdot \ln(2)}}. \tag{2.38}$$

Contrast Features

Contrast Features emphasize the differences between the useful signal produced by the target, enclosed in the *signal area*, and the background spread signal, enclosed in the *clutter area*. As shown in Fig. 2.6, we define signal and clutter areas as concentric ellipses centered in the centroid, with axes length:

Signal:

$$a(\rho, \phi) \leq 3 \cdot \sigma(\rho, \phi) \tag{2.39}$$

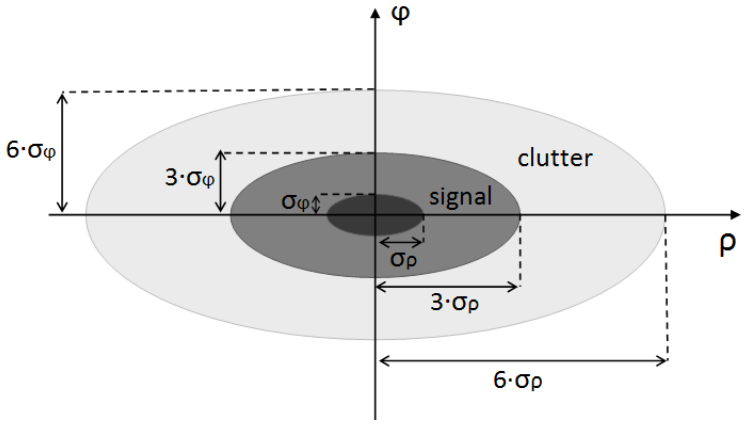

Figure 2.6: Signal and Clutter ellipses centered in centroid, in ρ, ϕ coordinate system.

Clutter:

$$3 \cdot \sigma_{\rho,\phi} < a_{\rho,\phi} < 6 \cdot \sigma_{\rho,\phi} \tag{2.40}$$

where σ is standard deviation, see (2.38). We define Contrast Features in terms of:

Signal-to-Clutter Ratio:

$$SCR = \frac{\max\limits_{\boldsymbol{r}_i \in \text{ signal}} \{\phi(\boldsymbol{r}_i)\}}{\max\limits_{\boldsymbol{r}_i \in \text{ clutter}} \{\phi(\boldsymbol{r}_i)\}} \tag{2.41}$$

Signal-to-Clutter Mean Ratio:

$$SCMR = \frac{\frac{1}{N_s} \sum\limits_{\boldsymbol{r}_i \in \text{ signal}} \phi(\boldsymbol{r}_i)}{\frac{1}{N_c} \sum\limits_{\boldsymbol{r}_i \in \text{ clutter}} \phi(\boldsymbol{r}_i)} \tag{2.42}$$

where ϕ_i is signal value, N_s and N_c are number of points in Signal and Clutter areas, respectively.

Chapter 3

Scatterer Detection

The objective is to reconstruct a point scatterer, which represents the tumor, embedded in a circular domain, which represents breast tissue, using the imaging algorithm described in the previous Chapter. The data used in the reconstruction derive from simulation performed with `COMSOL − Multiphysics` software.

The first part of this chapter describes the system architecture created in COMSOL simulation software; in the second one the reconstruction of the system with imaging algorithm is shown, then the reconstruction performance of the algorithm is analyzed varying the following parameters:

- Working frequency,
- Tumor position,
- Tumor size,
- Tumor-background contrast,
- Breast size,
- Unknown breast properties.

3.1 Simulation Process

The reconstruction has been achievable through the synthetic data provided from computer simulations. The computer simulations allow us to analyze the behaviour of the system under test in different parameter configurations. Moreover, they are very important to perform a sensitivity analysis for the validation of the experimental results. The computer simulations are performed with `COMSOL − Multiphysics` simulation software. Before presenting the software, we want to briefly explain the mathematical technique on which it is based: the finite element method.

3.1.1 Finite element method

The finite element method (FEM) is a numerical technique for finding approximate solutions to boundary value problems for partial differential equation [41]. The development of the finite element method dates in the second half of the '50s with the fundamental contribution of M.J. Turner and R.W. Clough [42].

The process is illustrated in fig. 3.1, it begins with a synergy of physical system

description and mathematical model formulation [43]. The mathematical model is often an ordinary differential equation (ODE), or a partial differential equation (PDE) in space and time. The processes of idealization and modelling are carried out concurrently to produce the discrete model. The solution step is handled by an equation solver often customized to FEM, which delivers a discrete solution (or solutions). The concept of error arises when the discrete solution is found, it is the amount by which the discrete solution fails to satisfy the mathematical model.

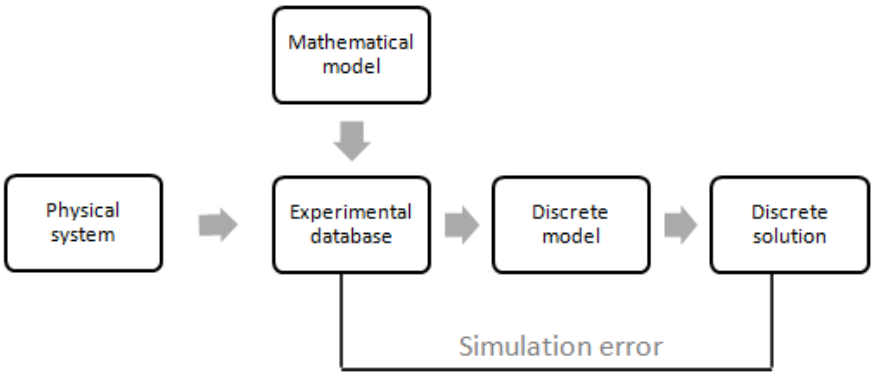

Figure 3.1: Model updating process in the The finite element method (FEM).

FEM Solution Process :

1. Divide structure into pieces (elements with nodes) (discretization/meshing)
2. Connect (assemble) the elements at the nodes to form an approximate system of equations for the whole structure (forming element matrices)
3. Solve the system of equations involving unknown quantities at the nodes (e.g., displacements)
4. Calculate desired quantities (e.g., strains and stresses) at selected elements

The basic concept in the physical FEM is the discretization of the continuous domain into disjoint (non-overlapping) components of simple geometry called *finite elements*. The built discrete domain is called *mesh*. Each element is expressed in terms of a finite number of Degrees Of Freedom (DOF) characterized as the value of an unknown function (force function), at a set of nodal points. The response of the mathematical model is then considered to be approximated by that of the discrete model obtained by connecting or assembling the collection of all elements. The key thing to remember is that Boundary Conditions (BCs) come in two basic flavours: *essential* BCs directly affect DOFs and are imposed conditions on the node vector, *natural* BCs do not directly affect DOFs and are imposed the force vector.

3.1.2 COMSOL-Multiphysics

`COMSOL – Multiphysics` is a general-purpose software platform, based on advanced numerical methods, for modelling and simulating physics-based problems. It is a finite element analysis, solver and Simulation software / FEA Software package for various physics and engineering applications, especially coupled phenomena,

or multiphysics. Several add-on products are available for COMSOL − Multiphysics, these have been categorized according to the applications areas, namely: Electrical, Mechanical, Fluid, Chemical.

We use the Electrical applications, in particular the AC/DC Module, which is used for simulating electric, magnetic, and electromagnetic fields in static and low-frequency applications. We use COMSOL − Multiphysics to solve the inverse scattering method and the Helmholtz differential equation, see § 2.2. The simulation process can be divided into three steps: building of the system geometry, parameters setting, mesh building.

The System Geometry

The software has an internal graphics, CAD-style, for the geometry creation in 1D, 2D and 3D, furthermore it can import geometry created by outside design tools. The geometry system is composed of five elements: the breast, the skin layer, the tumor, the dipole antenna and the coupling medium.

The breast is a circular investigation domain centered in the system origin, its radius is r_b and it is characterized by ε_b relative permittivity and Debye electrical parameters equal to $[\varepsilon_{\infty,b},\ \Delta\varepsilon_b,\ \tau_b(\text{ps}),\ \sigma_\text{b}(\text{S/m})]$. An outer skin layer is included, its thickness and its permittivity are t_s and ε_s, at which is associated $[\varepsilon_{\infty,s},\ \Delta\varepsilon_s,\ \tau_s(\text{ps}),\ \sigma_\text{s}(\text{S/m})]$ Debye parameters. The target to be detected (tumor) has radius r, is characterized by ε permittivity with $[\varepsilon_\infty,\ \Delta\varepsilon,\ \tau(\text{ps}),\ \sigma(\text{S/m})]$ and it is located at point $\boldsymbol{X}$ with respect to the origin of the circular geometry. The electric field $\boldsymbol{E}$ is collected by a dipole antenna over n_a positions: $\boldsymbol{R}_i = \boldsymbol{R}_1, ..., \boldsymbol{R}_{n_a}$ taken uniformly over a concentric (with the breast) circle of radius $r_{ap} > r_b$. The antenna system is in monostatic configuration, this means that the same antenna transmits and receives. The breast (with the skin) and the antenna element are embedded in a coupling medium with ε_d and $[\varepsilon_{\infty,d},\ \Delta\varepsilon_d,\ \tau_d(\text{ps}),\ \sigma_\text{d}(\text{S/m})]$ electrical properties.

The 3D structure system is created extruding the 2D structure along z-axis. In particular breast, skin and coupling medium are extruded for 4λ (wavelength) along z-axis, and antenna for $\lambda/4$. The figure 3.2a shown the 3D structure. The domain is inclosed in a sphere which represents the *Perfectly Matched Layer* (PML). The PML is an artificial absorbing layer for wave equations without field reflection, here is used to truncate finite element computational region.

RF module and Physical Parameters

A tool of COMSOL software is dedicated at parameters specification: property of the material and physic constant values. It accepts numeric and vector values, but also mathematical expression. Each element of the considered system is defined in the parameter specification tool. The parameter specification is shown in Table 3.1. This parameter configuration represents the operation point. During the simulation this parameter configuration is modified to study the behaviour of the system and the results are compared with the operating point ones.

Table 3.1: The parameters of the operating point for each element. (*) values with reference to: Zastrow et al. [38]. (**) values with reference to: Li et al. [12].

Parameter	Symbol	Value/Expression
breast radius	r_b(mm)	48
breast rel. permettivity	ε_b	5.1
breast Debye par.	$[\varepsilon_{\infty,b},\ \Delta\varepsilon_b,\ \tau_b(ps),\ \sigma_{\mathrm{b}}(S/m)]$	$[3.2,\ 1.9,\ 13,\ 0.05]$
skin layer thickness	t_s(mm)	2
skint rel. permettivity	ε_s	36
skin layer Debye par.	$[\varepsilon_{\infty,s},\ \Delta\varepsilon_s,\ \tau_s(ps),\ \sigma_{\mathrm{s}}(S/m)]$	$[16,\ 24,\ 13,\ 0.81]^*$
tumor radius	r(mm)	2.5
tumor rel. permettivity	ε	50
tumor Debye par.	$[\varepsilon_\infty,\ \Delta\varepsilon,\ \tau$(ps)$,\ \sigma$(S/m)$]$	$[4,\ 46,\ 6,\ 0.7]^{**}$
tumor position	$\boldsymbol{X}$(mm)	$[25, 0]$
radius antenna	r_a(mm)	2
frequency	ν(GHz)	2.4
n$^{\mathrm{o}}$ of ant. position	n_a	20
radius ant. position	r_{ap}(mm)	55
i-th ant. angle	α_i(rad.)	$i \cdot 2\pi/n_a,\ \forall i = 1, \ldots, n_a$
i-th ant. position	$\boldsymbol{R}_i$(mm)	$[r_{ap} \cdot \cos(\alpha_i),\ r_{ap} \cdot \sin(\alpha_i)]$
coupling medium radius	r_d(mm)	100
coup. med. rel. permet.	ε_d	5
coup. med. Debye par.	$[\varepsilon_{\infty,d},\ \Delta\varepsilon_d,\ \tau_d(ps),\ \sigma_{\mathrm{d}}(S/m)]$	$[3,\ 2,\ 13,\ 0.05]$

The Mesh

The mesh, as above-mentioned, is the discrete domain obtained through the FEM. The figure 3.2b shows the system mesh, it is composed of triangular elements: three nodes are joined by three edge, the edges can be straight or curvilinear. In 3D configuration, triangular elements are modified in tetrahedra elements. The mesh setting parameter are λ-dependent and are optimized by the software.

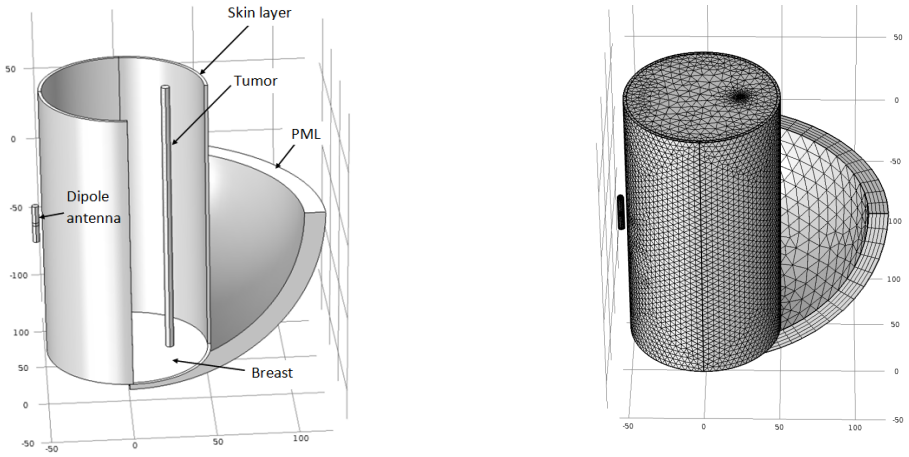

(a) The system geometry and system elements: breast, skin layer, tumor, dipole antenna and coupling medium.

(b) The mesh: discretization of domain with triangular finite elements.

Figure 3.2: The system geometry and the mesh structure built in `COMSOL – Multiphysics` software.

3.2 The Operating Point

Consider the operation point of Table 3.1 in § 3.1.2. The computer simulation returns the value of the $\boldsymbol{S}_{11}$ reflection parameter, collected by a dipole antenna over 20 positions ($\boldsymbol{R} = \boldsymbol{R}_1, ..., \boldsymbol{R}_{20}$) for a set of frequencies. The values of the reflection parameter are given as input to the imaging algorithm to obtain reconstructions. The algorithm works on a 2-D slice of the breast, though the operations can be extended to more slices and then the results can be combined to obtain a 3-D reconstruction. Here, we discuss 2D reconstructions only. The position of the source is identified by the peak of *pseudospectrum*, defined as:

$$\phi = \frac{1}{1 - \|cos_{ks}\eta\|^2}. \tag{3.1}$$

An example of pseudospectrum image is shown in figure 3.3. The imaging algorithm identifies the scatter position at the point: C(x,y)=(25.5, 0.2)mm. The goodness of the reconstruction is assessed by means of the metrics, Table 3.2.

The algorithm detects the target position and computes the metrics in deterministic manner. The value and the error in tab. 3.2 are the mean values and

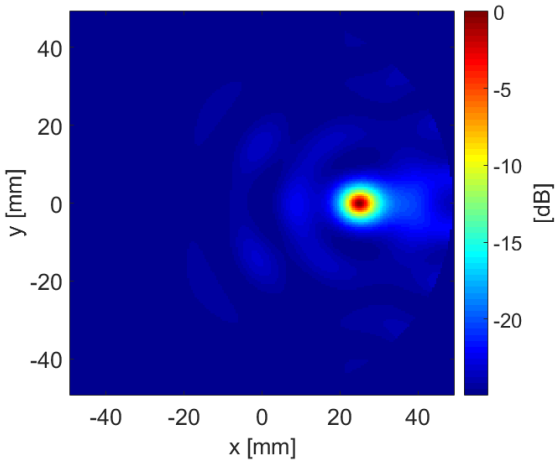

Figure 3.3: The resulting pseudospectrum at $\nu = 2.4$ GHz. Barcolor: from red color, high value in dB, to blue, low values.

Table 3.2: Spatial and contrast metrics for the pseudospectrum at $\nu = 2.4$ GHz.

Spatial metrics						Contrast metrics	
FWHM$_\rho$[mm]	SD$_\rho$[mm]	p-value$_\rho$	FWHM$_\phi$[mm]	SD$_\phi$[mm]	p-value$_\phi$	SCR[dB]	SCMR[dB]
7.8 ± 0.7	0.5 ± 0.3	0.89	6.5 ± 0.4	0.01 ± 0.01	1.00	17 ± 2	9.0 ± 0.5

standard errors computed on ten measurements after we have perturbed the system with white Gaussian noise (SNR=10dB), they write as:

$$\overline{x} = \frac{1}{N_m}\sum_{i=1}^{N_m} x_i \qquad se_x = \frac{\sigma_x}{\sqrt{N_m}} \tag{3.2}$$

where x_i represents the i-th value of a generic metric, σ_x is the standard deviation and $N_m = 10$ is the number of repeated measurements.

The reconstruction performance of the algorithm are analyzed varying the operating point in the following parameters: working frequency, tumor position, tumor size, tumor-background contrast, breast size and unknown breast electrical properties.

3.2.1 Working Frequency

The objectives are: to identify and locate the point scatterer varying the working frequency, to evaluate the reconstructions and finally to select the best frequency range.

The working conditions are the same of the operating point: Table 3.1 in § 3.1.2. In this case the electric field is generated in `COMSOL` at different frequencies. The frequency range is from $\nu = 1$GHz to $\nu = 5$GHz. Some examples of pseudospectra, as a function of the varying frequency, are shown in figure 3.4.

Observing the image series in Figure 3.4, it can be seen that as frequency increases PSF-pseudospectrum diminished in size, this effect is due to the improvement of the spatial resolution. However, at high frequencies we note some

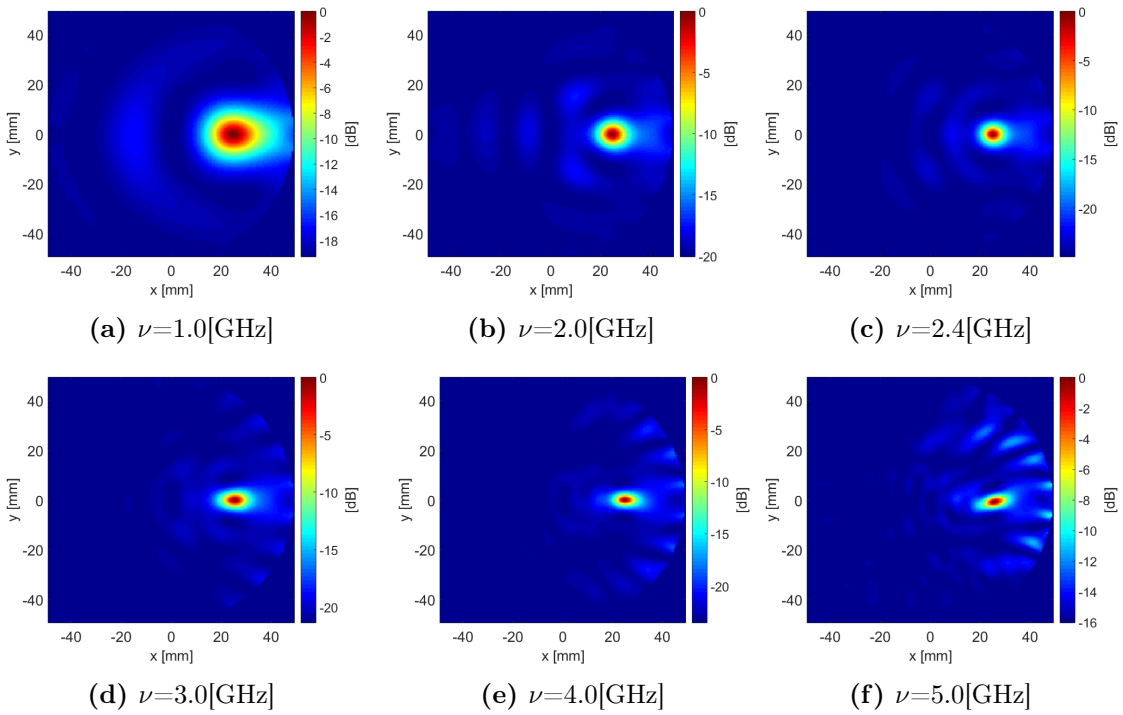

(a) ν=1.0[GHz] **(b)** ν=2.0[GHz] **(c)** ν=2.4[GHz]

(d) ν=3.0[GHz] **(e)** ν=4.0[GHz] **(f)** ν=5.0[GHz]

Figure 3.4: Pseudospectra frequency evolution, from ν=1GHz to ν=5GHz. Barcolor: from red color, high value in dB, to blue, low values.

secondary peaks, it implies that the algorithm creates artefacts in the pseudospectrum.

In order to evaluate the reconstructions and to select the best frequency range, some metrics are computed as described in § 2.4.3.

Spatial Metrics

In Table 3.3, the spatial metrics along ρ and ϕ axes at different frequencies are summarized; in figures 3.5 and 3.6 their trends are plotted.

Table 3.3: Spatial Metrics as a function of frequency.

ν[GHz]	FWHM$_\rho$[mm]	SD$_\rho$[mm]	p-value$_\rho$	FWHM$_\phi$[mm]	SD$_\phi$[mm]	p-value$_\phi$
1.0	18.2 ± 1.2	1.4 ± 0.7	0.86	14.1 ± 0.7	0.02 ± 0.02	0.99
2.0	12.9 ± 0.5	1.0 ± 0.3	0.86	9.0 ± 0.3	0.00 ± 0.01	1.00
3.0	10.1 ± 0.3	0.7 ± 0.2	0.68	5.9 ± 0.1	0.02 ± 0.01	0.99
4.0	10.0 ± 0.6	0.5 ± 0.3	0.91	5.0 ± 0.1	0.02 ± 0.01	0.99
5.0	9.8 ± 0.3	1.1 ± 0.1	0.79	4.6 ± 0.1	-0.02 ± 0.01	0.99

The metrics FWHM$_\rho$ and FWHM$_\phi$ confirm that as frequency increases the spread of the PSF-pseudospectrum reduces. In particular, in the range from 1GHz to 2GHz, the spread is halved, from 2GHz to 5GHz it decreases slowly. The FWHM outcomes depend also on the size of the scatterer, remember scatterer radius: $r = 2.5mm$.

The SD metrics is a measure of the error committed by the algorithm in target localization. The SD$_\rho$ metric underlines a large localization error along the ρ

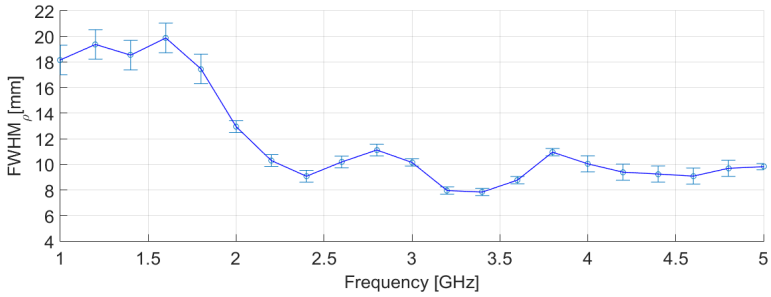

(a) FWHM$_\rho$-metric

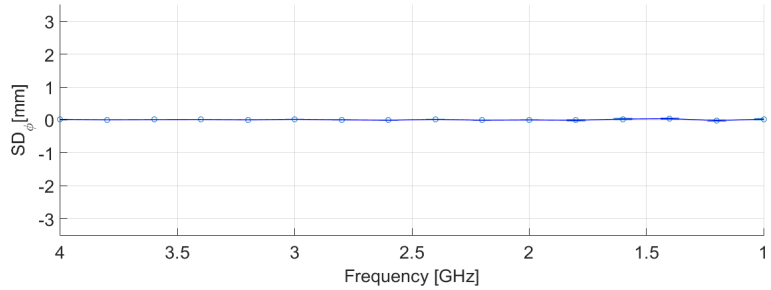

(b) SD$_\rho$-metric

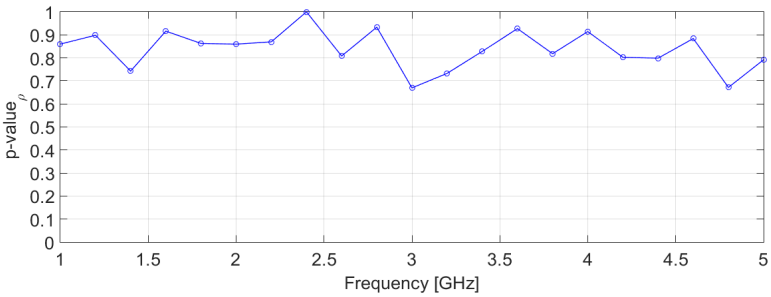

(c) p-value$_\rho$-metric

Figure 3.5: Spatial Metrics, radial direction.

direction at low frequency. The p-value$_\rho$, which represents an significance index of correct localization, is lower than 0.8 for $\nu < 2$GHz, in the range [2,4]GHz is 0.9 than 4GHz returns to 0.8. Along ϕ direction, the error is very small (lower 0.1 mm) and p-value$_\phi$ is about 0.99 always, it is due to circular symmetry of the measuring system.

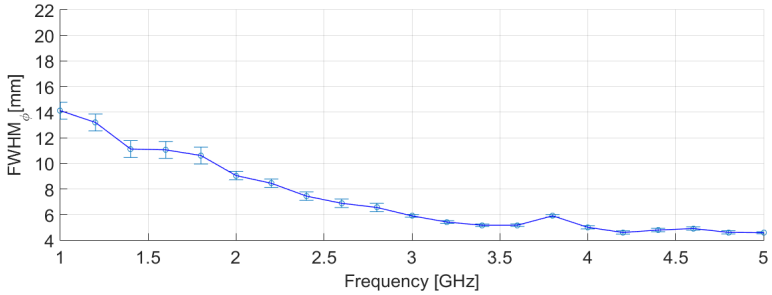

(a) FWHM$_\phi$-metric

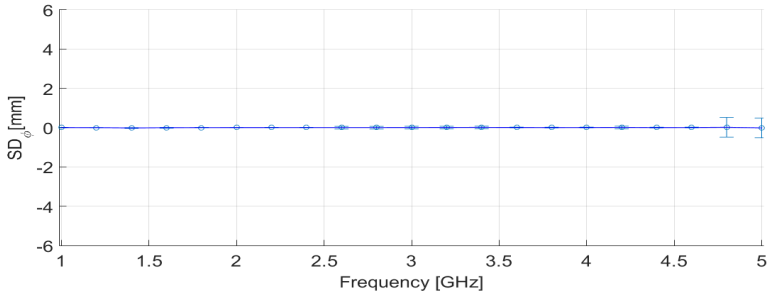

(b) SD$_\phi$-metric

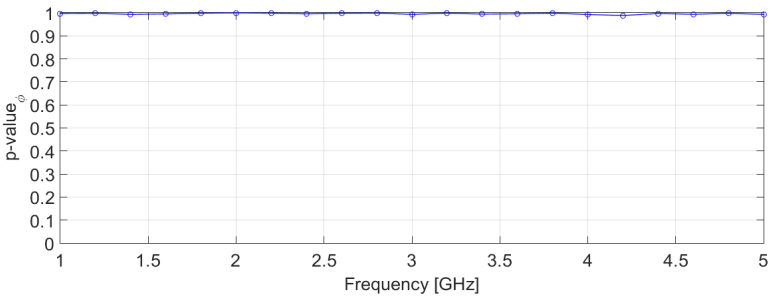

(c) p-value$_\phi$-metric

Figure 3.6: Spatial Metrics, angular direction.

The small error committed by the algorithm and the weak spread of PSF-pseudospectrum agree to select the $\nu = [2, 5]$GHz as best frequency range. The mean significance level in this frequency range is 80% in ρ-direction and 99% in ϕ-direction.

Contrast Metrics

In Table 3.4, the contrast metrics at different frequencies are summarized; in figures 3.7 their trends are plotted, particular fig. 3.7a SCR-metric and fig. 3.7b SCMR-metric.

The SCR-metric is a measure of the absolute ratio between max value in signal area and the max value in clutter area. This ratio increases up to 4GHz, then

decreases. Low values of SCR at low frequency indicates a small value of absolute signal maximum, thus a weak signal value, instead low values of SCR at high frequency indicates the presence of strong artefacts that disrupts the pseudospectrum.

The SCMR-metric is defined as the ratio between mean value in signal area and mean value in clutter area. The SCMR-trend is similar to SCR-trend, but smoother and lower. It defines the relative contrast of the two areas. By comparing contrast metrics, we conclude that until 2GHz clutter value are low, but also signal value are low, in the range $\nu = [2, 4]$GHz we have the higher ratio, over 4GHz clutter value are relevant.

Table 3.4: Contrast Metrics as a function of frequency.

ν[GHz]	SCR[dB]			SCMR[dB]		
1.0	8.9	$\pm$	1.9	4.3	$\pm$	0.6
2.0	9.7	$\pm$	1.0	4.6	$\pm$	0.5
3.0	13.1	$\pm$	0.4	6.5	$\pm$	0.2
4.0	12.3	$\pm$	0.3	5.6	$\pm$	0.2
5.0	6.9	$\pm$	0.4	3.6	$\pm$	0.3

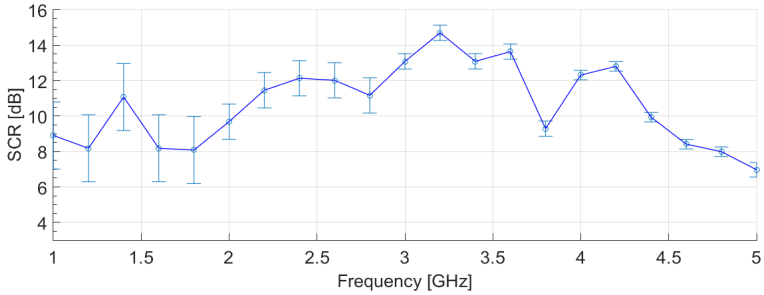

(a) SCR-metric

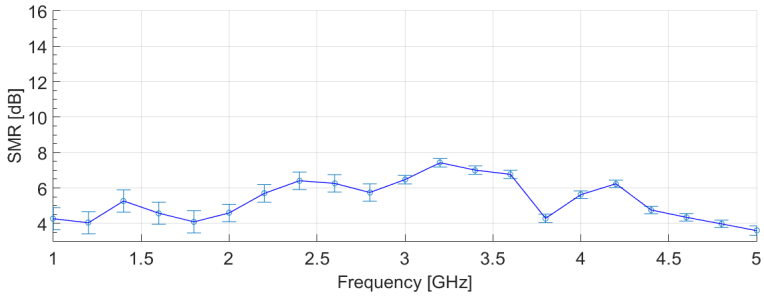

(b) SCMR-metric

Figure 3.7: Contrast Metrics.

GM-MUSIC Psedospectrum

As shown above, a single-frequency approach suffers from the tradeoff between high resolution and artefact limitations. Data collected at different frequencies can be employed to improve the performance of the single-frequency case. The

frequency information can be combined in the GM-MUSIC method, see § 2.3.4. The resulting GM-MUSIC pseudospectrum, using the selected frequency range $\nu = [2, 4]$GHz, is shown in figure 3.8.

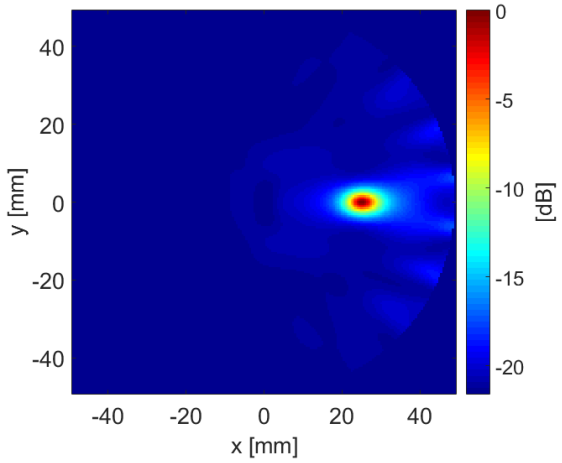

Figure 3.8: The resulting GM-MUSIC pseudospectrum with $\nu = [2, 4]$GHz. Barcolor: from red color, high value in dB, to blue, low values.

The computed metrics are specified in the Table 3.5.

Table 3.5: Spatial and contrast metrics for GM-MUSIC pseudospectrum with $\nu = [2, 4]$GHz.

Spatial metrics						Contrast metrics	
FWHM$_\rho$[mm]	SD$_\rho$[mm]	p-value$_\rho$	FWHM$_\phi$[mm]	SD$_\phi$[mm]	p-value$_\phi$	SCR[dB]	SCMR[dB]
9 ± 1	0.8 ± 0.1	0.89	6.4 ± 0.5	0.01 ± 0.01	1.00	16 ± 1	8.1 ± 0.1

The GM-MUSIC contrast metrics have higher values than the single-frequency case, this is because GM-MUSIC algorithm enhances the signal area and averages the clutter area in the pseudospectrum, it also improves the spatial resolution, indeed the pseudospectrum has a lower spread and a more accurate scatterer localization. The GM-MUSIC metric errors are defined as the standard errors computed on ten measures after we have perturbed the system with white Gaussian noise (SNR=10dB), as in eq. (3.2) of § 3.2.

3.2.2 Tumor Position

The objective is to identify and locate the point scatterer varying its position, than to evaluate the reconstructions. As shown in § 3.2, the angular direction of the scatterer is accurately detected due the circular symmetry, so we focus on the radial direction. We choose three scatterer position under the test:

near center: $\boldsymbol{X} = (10, 0)$ mm;
half radius: $\boldsymbol{X} = (25, 0)$ mm;
near skin: $\boldsymbol{X} = (40, 0)$ mm.

For each position are obtained pseudospectra at different frequencies and then are combined with GM-MUSIC algorithm. The resulting GM-MUSIC pseudospectra,

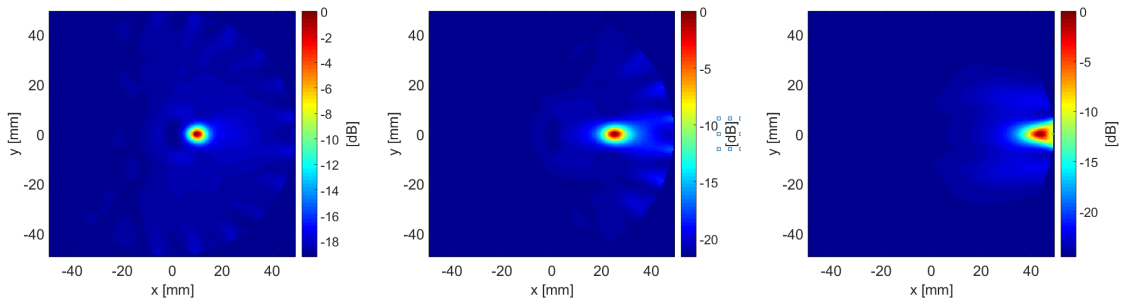

(a) near center **(b)** half radius **(c)** near skin

Figure 3.9: The resulting GM-MUSIC pseudospectra at different scatterer position, $\nu = [2, 4]$GHz. Barcolor: from red color, high value in dB, to blue, low values.

using the frequency range $\nu = [2, 4]$GHz, are compared in figure 3.9 and the computed metrics are specified in Table 3.6. From the study of the metrics we can conclude that the algorithm performance degrades gradually you get closer to the edges of the breast, this happens because the measure is affected by skin reflections near the edges. The best position is scatterer near the center of the breast, because it is the most symmetrical position. We must consider near skin as a borderline position, nevertheless, the algorithm detects the scatterer with 40% p-value confidence along the radial direction and 99% along that angle direction.

Table 3.6: Spatial and contrast metrics for GM-MUSIC pseudospectrum at different scatterer position.

	Spatial metrics												Contrast metrics					
	$FWHM_\rho$[mm]			SD_ρ[mm]			p-value$_\rho$	$FWHM_\phi$[mm]			SD_ϕ[mm]			p-value$_\phi$	SCR[dB]			SCMR[dB]		
near center	6	±	1	0.2	±	0.1	0.95	6.1	±	0.5	0.00	±	0.01	1.00	17	±	1	9.5	±	0.1
half radius	9	±	1	0.8	±	0.1	0.89	6.4	±	0.5	0.01	±	0.01	1.00	16	±	1	8.1	±	0.1
near skin	11	±	1	4.4	±	0.5	0.37	7.2	±	0.5	0.02	±	0.01	0.99	15	±	1	4.1	±	0.1

3.2.3 Tumor Size

The objective is to identify and locate the scatterer varying its size. We want

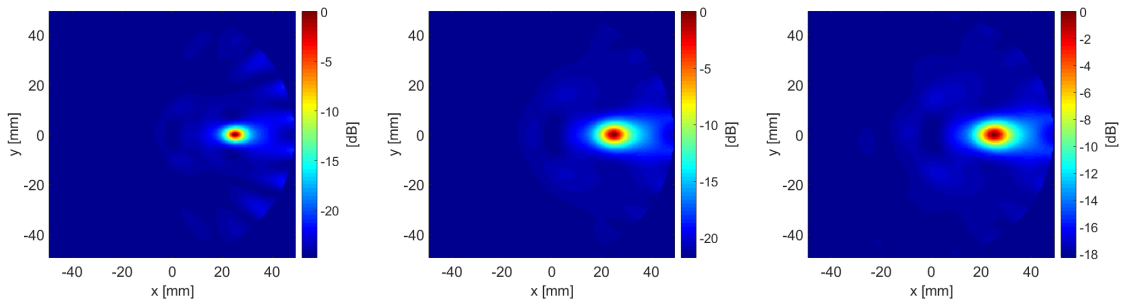

(a) Small tumor **(b)** Medium tumor **(c)** Large tumor

Figure 3.10: The resulting GM-MUSIC pseudospectra at different tumor sizes, $\nu = [2, 4]$GHz. Barcolor: from red color, high value in dB, to blue, low values.

to test the algorithm when the scatter is larger than 2.5mm-diameter. We choose three tumor size:

small tumor: $r = 2.5$mm;
medium tumor: $r = 5$mm;
large tumor: $r = 7.5$mm.

The resulting GM-MUSIC pseudospectra of each tuomor, computed using the frequency range $\nu = [2, 4]$GHz, are compared in figure 3.11 and the relative metrics are specified in the Table 3.8. From the study of the metrics we note that the algorithm locates the scatter regardless of its size. The FWHM increases with the tumor size, this result is obvious because the FWHM is related to target size. We also note that at spread increasing the signal reduces, in fact the contrast metrics decrease with the tumor size.

Table 3.7: Spatial and contrast metrics for GM-MUSIC pseudospectrum at different tumor sizes.

	Spatial metrics												Contrast metrics					
	$FWHM_\rho$[mm]			SD_ρ[mm]			p-value$_\rho$	$FWHM_\phi$[mm]			SD_ϕ[mm]			p-value$_\phi$	SCR[dB]			SCMR[dB]		
small tumor	9	±	1	0.8	±	0.1	0.89	6.4	±	0.5	0.01	±	0.01	1.00	16	±	1	8.1	±	0.1
med. tumor	12	±	1	0.4	±	0.1	0.94	7.1	±	0.5	0.01	±	0.01	1.00	17	±	1	6.2	±	0.1
large tumor	13	±	1	0.8	±	0.1	0.87	8.2	±	0.5	0.01	±	0.01	0.99	14	±	1	5.4	±	0.1

3.2.4 Tumor-Background Contrast

The objective is to identify and locate the point scatterer varying the electrical contrast between the background medium and the scatterer. We want to test

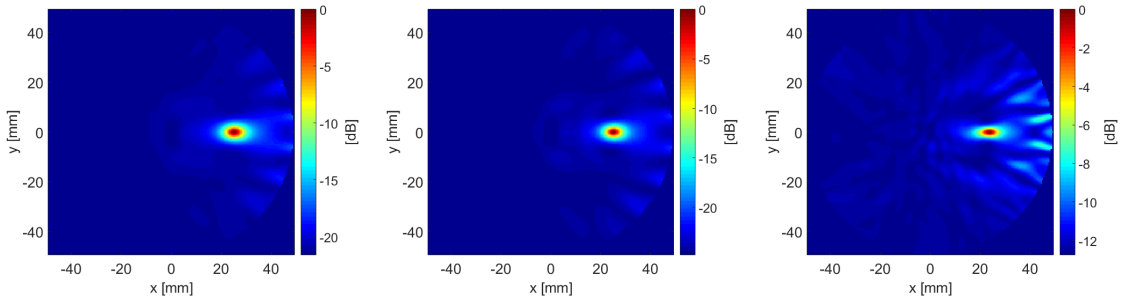

(a) High contrast **(b)** Medium contrast **(c)** Low contrast

Figure 3.11: The resulting GM-MUSIC pseudospectra at different tumor-background contrast, $\nu = [2, 4]$GHz. Barcolor: from red color, high value in dB, to blue, low values.

the algorithm when the medium, in which scatterer is embedded, changes. We choose three test tissue: fat tissue, intermediate tissue, fibroglandular tissue. The permittivity and the Debye parameters for each tissue are:

fat: $\varepsilon_b = 5.1$ with $\varepsilon_{\infty,b}$=3.2, $\Delta\varepsilon_b$=1.9, τ_b=13 ps, σ_b= 0.050 S/m;
intermediate: $\varepsilon_b = 10$ with $\varepsilon_{\infty,b}$=7.0, $\Delta\varepsilon_b$=3.0, τ_b=13 ps, σ_b= 0.15 S/m;
fibroglandular: $\varepsilon_b = 36$ with $\varepsilon_{\infty,b}$=12, $\Delta\varepsilon_b$=24, τ_b=13 ps, σ_b= 0.4 S/m.

The scatter electrical properties are fixed, $\varepsilon = 50$ with $[\varepsilon_\infty,\ \Delta\varepsilon,\ \tau(\text{ps}),\ \sigma(\text{S/m})] = [4,\ 46,\ 6,\ 0.7]$, instead medium properties varying with tissue composition, it

occurs that the contrast between the electrical properties of medium and scatterer decreases:

$$\begin{aligned} \text{fat} : \text{tumor} &= 1 : 10; \\ \text{intermediate} : \text{tumor} &= 1 : 5; \\ \text{fibroglandular} : \text{tumor} &= 3 : 5. \end{aligned}$$

So, we have high contrast between tumor and fat tissue, medium contrast for intermediate tissue (1:5), low contrast for fibroglandular tissue(3:5). For each tissue are obtained pseudospectra at different frequencies and then are combined with GM-MUSIC algorithm. The resulting GM-MUSIC pseudospectra, using the frequency range $\nu = [2, 4]$GHz, are compared in figure 3.11. The computed metrics are specified in the Table 3.8. From the study of the metrics we can conclude that the algorithm performance is equal for high and medium contrasts and degrades for low contrast; in particular we notes an increasing in delocalization and an halving in contrast metrics.

Table 3.8: Spatial and contrast metrics for GM-MUSIC pseudospectrum at different medium-scatterer electrical contrast.

	Spatial metrics						Contrast metrics	
	FWHM_ρ[mm]	SD_ρ[mm]	p-value_ρ	FWHM_ϕ[mm]	SD_ϕ[mm]	p-value_ϕ	SCR[dB]	SCMR[dB]
high contrast	9 ± 1	0.8 ± 0.1	0.89	6.4 ± 0.5	0.01 ± 0.01	1.00	16 ± 1	8.1 ± 0.1
med. contrast	9 ± 1	0.6 ± 0.1	0.86	5.4 ± 0.5	0.00 ± 0.01	1.00	17 ± 1	8.1 ± 0.1
low contrast	9 ± 1	-1.1 ± 0.1	0.77	4.1 ± 0.5	0.01 ± 0.01	1.00	8 ± 1	4.2 ± 0.1

3.2.5 Breast Size

The objective is to identify and locate the point scatterer varying the breast size. The breasts are also heterogeneous in size, so we consider three test classes

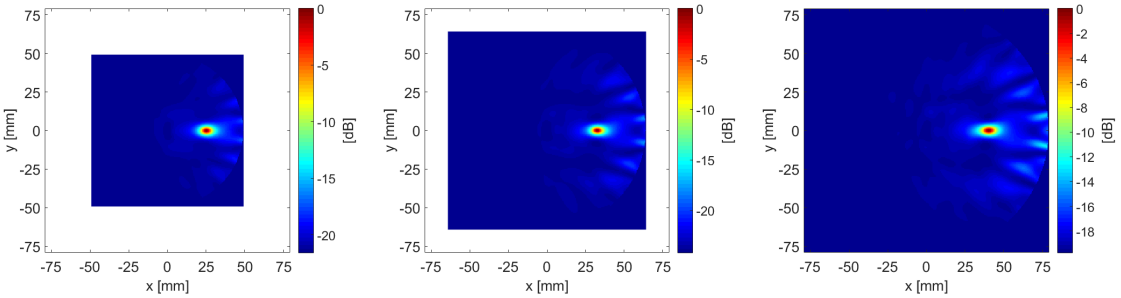

(a) small breast size **(b)** medium breast size **(c)** large breast size

Figure 3.12: The resulting GM-MUSIC pseudospectra at different breast sizes, $\nu = [2, 4]$GHz. Barcolor: from red color, high value in dB, to blue, low values.

in order to evaluate the differences between the various size:

$$\begin{aligned} \text{small breast size:} &\ r_b{=}50\text{mm}, \\ \text{medium breast size:} &\ r_b{=}65\text{mm}, \\ \text{large breast size:} &\ r_b{=}80\text{mm}. \end{aligned}$$

The scatterer position remains at half radius, thus it proportionally changes with the breast size:

small breast size: $\boldsymbol{X}$=(25,0)mm,
medium breast size: $\boldsymbol{X}$=(32.5,0)mm,
large breast size: $\boldsymbol{X}$=(40,0)mm.

The electrical breast properties are these of the operating point. The resulting GM-MUSIC pseudospectra of each breast size, computed using the frequency range $\nu = [2, 4]$GHz, are compared in figure 3.11 and the relative metrics are specified in the Table 3.8. From the study of the metrics we can conclude that the algorithm retains the same performance at different breast sizes, this is because the medium is perfectly homogeneous.

Table 3.9: Spatial and contrast metrics for GM-MUSIC pseudospectrum at different medium-scatterer electrical contrast.

	Spatial metrics									Contrast metrics		
	FWHM_ρ[mm]	SD_ρ[mm]	p-value$_\rho$	FWHM_ϕ[mm]	SD_ϕ[mm]	p-value$_\phi$	SCR[dB]	SCMR[dB]
small breast	9 ± 1	0.8 ± 0.1	0.89	6.4 ± 0.5	0.01 ± 0.01	1.00	16 ± 1	8.1 ± 0.1
med. breast	9 ± 1	0.6 ± 0.1	0.86	5.1 ± 0.5	0.01 ± 0.01	1.00	16 ± 1	7.9 ± 0.1
large breast	9 ± 1	0.8 ± 0.1	0.89	5.9 ± 0.5	0.00 ± 0.01	1.00	13 ± 1	7.0 ± 0.1

3.2.6 Unknown Breast Properties

The objectives are: to identify and locate the point scatterer varying its breast electrical properties, than to evaluate the reconstructions and the errors.

Here, we consider the case where the background medium (still homogeneous) is not a priori known. This entails that medium's Debye parameters used in reconstruction are different from those assumed in Table 3.1 in § 3.1.2 and used in `COMSOL` simulation. We define two limits around the average Debye parameters

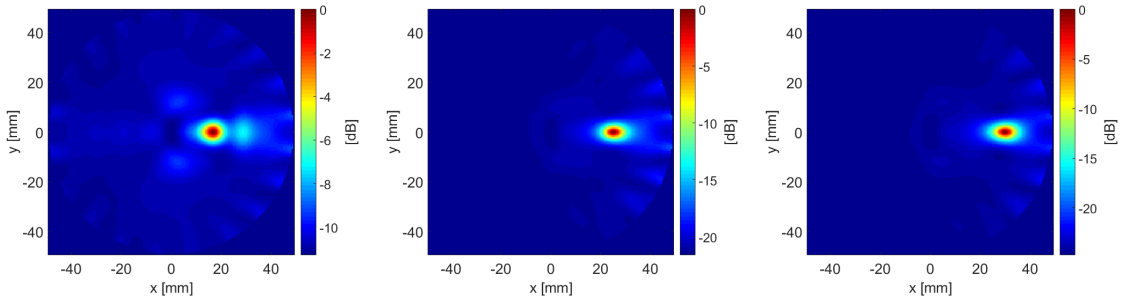

(a) lower limit **(b)** mean value **(c)** upper limit

Figure 3.13: The resulting GM-MUSIC pseudospectra at different Debye configuration parameters, $\nu = [2, 4]$GHz. Barcolor: from red color, high value in dB, to blue, low values.

found in § 3.2.6:

lower limit: $\varepsilon_b = 2.4$ with $\varepsilon_{\infty,b}$=2.3, $\Delta\varepsilon_b$=0.1, τ_b=13 ps, σ_b= 0.001 S/m;
mean value: $\varepsilon_b = 5.1$ with $\varepsilon_{\infty,b}$=3.2, $\Delta\varepsilon_b$=1.9, τ_b=13 ps, σ_b= 0.050 S/m;
upper limit: $\varepsilon_b = 8.2$ with $\varepsilon_{\infty,b}$=4.2, $\Delta\varepsilon_b$=4.0, τ_b=13 ps, σ_b= 0.100 S/m.

The limits are set with a confidence level equal to three standard deviations around the mean value and represent the statistical variability induced by the breast heterogeneity. The resulting GM-MUSIC pseudospectra of each Debye parameter

configuration, are compared in figure 3.13. The GM-MUSIC is computed using the frequency range $\nu = [2, 4]$GHz, the relative metrics are specified in the Table 3.10.

Table 3.10: Spatial and contrast metrics for GM-MUSIC pseudospectrum at different Debye configuration parameters.

	Spatial metrics						Contrast metrics	
	$FWHM_\rho$[mm]	SD_ρ[mm]	p-value$_\rho$	$FWHM_\phi$[mm]	SD_ϕ[mm]	p-value$_\phi$	SCR[dB]	SCMR[dB]
lower limit	9 ± 1	-8.3 ± 0.1	0.02	7.1 ± 0.5	0.13 ± 0.01	0.97	8 ± 1	3.8 ± 0.1
mean value	9 ± 1	0.8 ± 0.1	0.89	6.4 ± 0.5	0.01 ± 0.01	1.00	16 ± 1	8.1 ± 0.1
upper limit	9 ± 1	5.2 ± 0.1	0.18	6.2 ± 0.5	0.05 ± 0.01	1.00	15 ± 1	6.9 ± 0.1

As we can see, when the Debye parameters are inaccurate, the algorithm detects the scatterer in different position. It delocalizes only along the radial direction, but this error is crucial, in fact, the probabilities to identify the scatterer in ρ-direction are: 0.02 for lower limit and 0.2 for upper limit. Another interesting aspect is the orientation: when the Debye parameters are underestimated, the algorithm delocalizes outwards ($SD_\rho<0$), else it delocalizes inwards($SD_\rho>0$).

3.3 Unknown Parameter Solution

In the previous section we presented the performance analysis of the MUSIC algorithm: it reveals that a correct estimation of breast Debye parameters is crucial in scatterer detection. We have a correct reconstruction when the reconstruction parameters agrees with simulation one, besides a small variation in reconstruction parameter produces a large scatterer delocalization. In a real case, the correct reconstruction occurs when we know the anatomy of breast under the test. Unfortunately, the breast anatomy under the test is unknown and we know that Debye parameters vary due the breast heterogeneity, therefore a correct estimation is hard to achieve.

In order to minimize the error made when parameters are unknown, we exploit the only available information: the antenna measurements. The idea is to find the parameters that maximize Signal-to-Clutter Mean Ratio (SCMR) in the pseudospectrum. The figure 3.14 shows the values of the SCMR at the operating point, at one-, two-, three-sigma distance from the operating point. As we can see, the SCMR is maximum in the operating point and for this point the SD (localization error) is minimum. We want to use this information to find the reconstruction that minimizes the localization error.

The basic idea for improving the reconstruction algorithm is: moving away from the operating point, the reconstruction degrades and the algorithm delocalizes the target, our assumption is thus that the reconstruction has the least error when the SCMR is maximum. Now, the problem formulation becomes the minimization of the inverse of SCMR in the pseudospectra.

The optimization problem considered assumes the general form:

$$\min_{x \in X} f(x) \tag{3.3}$$

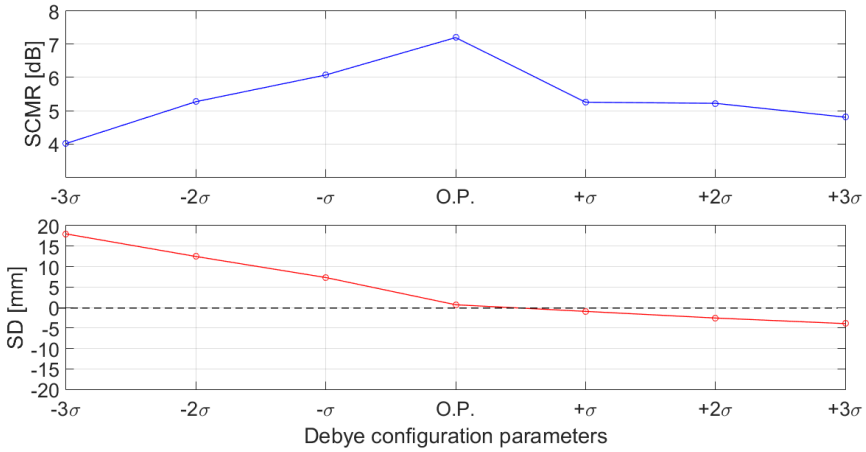

Figure 3.14: The SCMR-values of the pseudospectra obtained at the operating point, at one-, two-, three-sigma distance from the operating point, upside blue-line; the related SD-values, downside red-line.

where $f : \mathbb{R}^n \to \mathbb{R}^n$ is the cost function, $x \in X$ is the vector of design parameters and $X \subseteq \mathbb{R}^n$ is parameters subspace. In our problem formulation the cost function is the inverse of SCMR and x is the Debye parameter vector ($\varepsilon_{\infty,b}$, $\Delta\varepsilon_b$, τ_b, σ_b). The optimization problem is unconstrained, $X = \mathbb{R}$, this means that the Debye parameter vector can varies in $\mathbb{R}^n$.

The solution space appears with a lot of local minima, then the cost function can't be gradient-based. We use an optimization algorithm based on the pattern search [1] algorithm developed by Hooke and Jeeves [44] and improved by V.Torczon [45], which is defined for derivative-free unconstrained optimization on continuously differentiable functions using positive spanning directions.

3.3.1 The Optimizing Algorithms Choice

In order to choose the optimization method, we evaluated three of the most popular algorithms: the Genetic Algorithm (GA), The Simulated Annealing (SA) and the Pattern Search Method (PSM).

A Genetic Algorithm (GA) is a method for solving both constrained and unconstrained optimization problems based on a natural selection process that mimics biological evolution. The algorithm repeatedly modifies a population of individual solutions. At each step, the genetic algorithm randomly selects individuals from the current population and uses them as parents to produce the children for the next generation. Over successive generations, the population "evolves" toward an optimal solution [53].

Simulated Annealing (SA) is a method for solving unconstrained and bound-constrained optimization problems. The method models the physical process of heating a material and then slowly lowering the temperature to decrease defects, thus minimizing the system energy. At each iteration of the simulated annealing

[1] Genetic algorithm and simulated annealing algorithm are also test. We have chosen pattern search because it has higher performance and less computation time than other algorithms, see § 3.3.1.

algorithm, a new point is randomly generated. The distance of the new point from the current point, or the extent of the search, is based on a probability distribution with a scale proportional to the temperature. The algorithm accepts all new points that lower the objective, but also, with a certain probability, points that raise the objective. By accepting points that raise the objective, the algorithm avoids being trapped in local minima in early iterations and is able to explore globally for better solutions [54].

The Pattern Search Method (PSM) consists of a sequence of exploratory moves about a base point which, if successful, are followed by pattern moves. This method is extensively discussed in § 3.3.2.

The three algorithms are tested at the working conditions of the operating point (Table 3.1 in § 3.1.2) using the cost function defined in § 3.3.3 with tolerance sets at 10^{-4}dB. The outcomes are shown in Table 3.11.

Table 3.11: Spatial and contrast metrics for GM-MUSIC pseudospectrum at different tumor sizes.

	Spatial metrics												Contrast metrics						
	$FWHM_\rho$[mm]			SD_ρ[mm]			p-value$_\rho$	$FWHM_\phi$[mm]			SD_ϕ[mm]			p-value$_\phi$	SCR[dB]			SCMR[dB]			time[s]
PSM	17	±	1	-1.1	±	0.9	0.91	6.4	±	1.2	0.01	±	0.05	1.00	10	±	2	5.2	±	1.1	20± 2
GA	19	±	1	3.2	±	0.9	0.56	9.8	±	1.2	0.01	±	0.05	1.00	8	±	2	3.8	±	1.1	70± 3
SA	19	±	1	4.2	±	0.9	0.42	10.2	±	1.2	0.01	±	0.05	1.00	6.5	±	2	3.0	±	1.1	90± 3

The performances of the Pattern Search Method (PSM) are higher in spatial resolution, signal-to-noise ratio, scatter localization and also computation time.

3.3.2 Pattern Search Method

The Pattern Search Method (PSM) consists of a sequence of exploratory moves about a base point which, if successful, are followed by pattern moves. It proceeds evaluating the objective function in a point x_k belonging to a grid. The grid is independent from the objective function and is defined by a set of directions D_k and by a scalar $\Delta_k = x_k - x_{k+1}$ which indicates the distance between the grid-points. The idea is to evaluate the function $f(x)$ in the grid-neighbourhood of the current base point x_k. The move is equal to $s_k = D_k \cdot \Delta_k$. If any move is a success (i.e. results in a reduced function value), the new value of that variable will be retained. After all points have been considered, a new base point x_{k+1} will be reached. If $x_k \equiv x_{k+1}$, no function reduction has been achieved. The step length Δ_k is reduced and the procedure is repeated. If $x_k \not\equiv x_{k+1}$, a pattern move from x_k is made. A pattern move attempts to speed up the search by using the information already acquired about $f(x)$ so as to identify the best search direction. The new pattern point is given by:

$$p_k = x_k + 2 \cdot D_k \cdot \Delta_k \tag{3.4}$$

The search continues with a new sequence of exploratory moves about p_k. The minimum is assumed to be obtained when the step length for each variable has been reduced to a specified criterion value (Δ_{min}). The pseudo algorithm is:

Data: $x_k \in \mathbb{R}^n$, $\Delta_k > 0$ and $D_k \in \mathbb{R}^{n\times p}$, $p > 2n$;

Step 1: evaluate $f(x_k + D_k\Delta_k)$

if $f(x_k + D_k\Delta_k) < f(x_k)$, set $x_{k+1} = x_k + s_k$

else $x_{k+1} = x_k$

Step 2: update Δ_k and D_k

if $\Delta_k > \Delta_{min}$, set $x_k = x_{k+1}$ and go to **step 1**

else exit

In order to find minimum of the cost function using pattern search we exploit the MATLAB pattern search function. We use the syntax:

$$[\texttt{DebyeParam}, \texttt{minCF}] = \texttt{patternsearch}(\texttt{CostFunction}, \texttt{x}_0, \texttt{LB}, \texttt{UB}) \tag{3.5}$$

Where:

- `DebyeParam`: returns the Debye parameter vector which minimize the cost function;
- `minCF`: returns the minimum of cost function;
- `CostFunction`: is the input cost function, see 3.3.3;
- $\texttt{x}_0$: is the random initialization point;
- `LB`, `UB`: are the lower and upper parameter bounds.

The `LB`, `UB` conditions are non necessary and they have no effects on the solutions, but they are useful to reduce the computation time. The `LB`, `UB` bounds are not restrictive conditions, as we can see in Table 3.12, informations on the order of parameter magnitude are required.

Table 3.12: Ranges Debye configuration parameters.

	$\varepsilon_{\infty,b}$	$\Delta\varepsilon_b$	τ_b(ps)	σ_b (S/m)
min	1	0	13	0
max	100	100	13	1

3.3.3 The Cost Function

Due to the circular geometry and due to the dense number of antennas of the acquisition system, the angle of the position of the scatterer is always identified with a small error, see figure 3.15. We limit the reconstruction of the pseudospectrum along the line identified by the angle of the scatterer. We call this limited reconstruction: *linespectrum*. Now, the cost function maximizes the ratio between the maximum and the mean of the linespectrum. This operation causes information loss, but it considerably reduces the computation time. The Table 3.13 compares the results obtained maximizing the SCMR in the linespectrum and in the pseudospectrum. Using the linespectrum approximation, the reconstruction

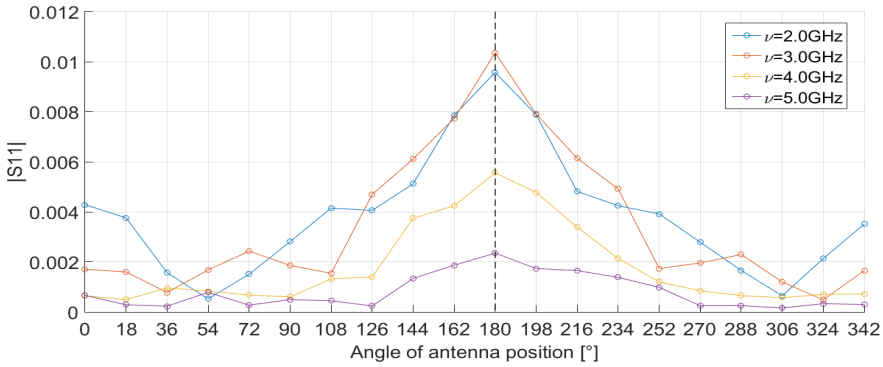

Figure 3.15: Filtered $|S_{11}|$ signal as a function of angle of antenna position. Signal examples at 2GHz, 3GHz, 4GHz and 5GHz. The maximum signal indicates the scatterer angle position, in the figure $\phi = 180°$.

Table 3.13: Spatial and contrast metrics for Eye-GMMUSIC linespectrum and Eye-GMMUSIC pseudospectrum.

	Spatial metrics						Contrast metrics	
	FWHM$_\rho$[mm]	SD$_\rho$[mm]	p-value$_\rho$	FWHM$_\phi$[mm]	SD$_\phi$[mm]	p-value$_\phi$	SCR[dB]	SCMR[dB]
pseudospectrum	12	1	0.80	5	0.01	1.00	11	7
linepseudospec.	15	1	0.89	5	0.01	1.00	10	6

loses in resolution (greater values of FWHM) and loses in contrast (lower values of SCR and SCMR). Such losses are assumed as acceptable since the location of the scatterer is not compromised and the computation time [2] is reduced by a factor:

$$\frac{t_p}{t_l} = \frac{6000 \text{ s}}{69 \text{ s}} \approx 100 \tag{3.6}$$

where t_p and t_l are Eye-GMMUSIC linespectrum and Eye-GMMUSIC pseudospectrum computation times, respectively.

Tolerance of the cost function is set at 10^{-4}dB, it defines the exit condition of the algorithm. The exit condition is satisfied after about 80 iterations, an example of the convergence of the cost function as a function of number of iterations, is shown in Fig. 3.16.

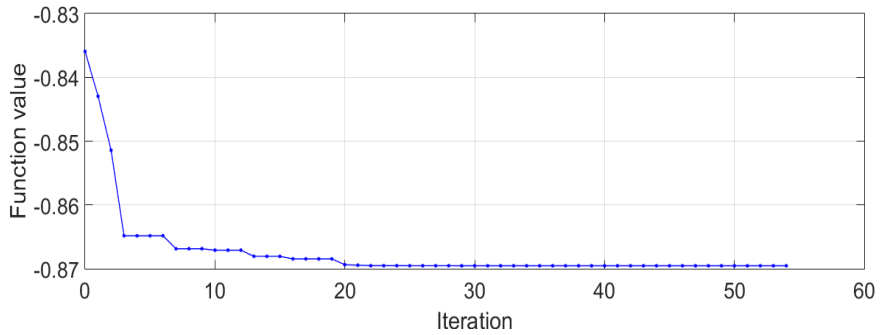

Figure 3.16: Cost function convergence as function a number of iterations.

[2]PC specification: Intel(R) Core(TM) i7-3770, CPU 3.40GHz, OS 64 bit and RAM 32GB.

3.3.4 The Eye-GMMUSIC algorithm

In the previous sections we presented all the basic components of the best reconstruction algorithm. Now, we want to merge the components and to provide the idea of the complete process. The process begins exploiting pattern search algorithm to find the Debye parameter vector that minimizes the inverse of SCMR. After that, we use the Debye vector to compute the reconstruction and to extract the relative pseudospectrum. This process is repeated for each frequency. At last, the obtained pseudospectra at different frequencies are combined with GMMUSIC algorithm. Despite the algorithm has no a priori information on the breast properties, it still "sees" the target about the correct position, so we have call this algorithmic process: Eye-GMMUSIC.

Step 1: pattern search algorithm $\rightarrow x = [\varepsilon_{\infty,b}, \Delta\varepsilon_b, \tau_b, \sigma_b]$ with $\min[f(x)]$;

Step 2: MUSIC with $x \rightarrow \Phi$ pseudospectrum ;

Step 3: repeat the previous steps for each frequency: $x_i \rightarrow \Phi_i$, $i = 1, ..N_\nu$

Step 4: GMMUSIC pseudospectrum $\Phi_{GM} = \sqrt[N_\nu]{\prod_{i=1}^{N_\nu} \Phi_i} \rightarrow$ target position

3.3.5 The Eye-GMMUSIC Results

Consider the system configuration: Table 3.1 in § 3.1.2. We know, from § 3.4, that the best performance of the reconstruction algorithm is in the frequency range $\nu = [2, 4]$GHz, so in this range we compute the Eye-GMMUSIC pseudospectrum performing the process of § 3.3.4. In order to construe the results, we compare the Eye-GMMUSIC and the GM-MUSIC obtained knowing the Debye parameters. The pseudospectra are compared in figure 3.17, the metrics in Table 3.14.

Table 3.14: Spatial and contrast metrics for GM-MUSIC vs. Eye-GMMUSIC.

	Spatial metrics												Contrast metrics					
	FWHM$_\rho$[mm]			SD$_\rho$[mm]			p-value$_\rho$	FWHM$_\phi$[mm]			SD$_\phi$[mm]			p-value$_\phi$	SCR[dB]			SCMR[dB]		
GM-MUSIC	9	±	1	0.8	±	0.1	0.89	6.4	±	0.5	0.01	±	0.01	1.00	16	±	1	8.1	±	0.1
Eye-GMMUSIC	17	±	1	-1.1	±	0.9	0.91	6.4	±	1.2	0.01	±	0.05	1.00	10	±	2	5.2	±	1.1

In Table 3.14, the outcomes of the two algorithm are compared. The performance of the Eye-GMMUSIC are lower than the GM-MUSIC: we notice a deterioration in the contrast and an increase in the spread. However, the principal task of Eye-GMMUSIC is to return the correct scatterer position, thus we will focus the analysis on the scatterer localization. We tested the algorithm in all conditions considered in § 3.2 and we provide a comparative analysis of the GMMUSIC and Eye-GMMUSIC outcomes. Assuming the GM-MUSIC as the best possible solution and computing the module of Spatial Displacement ($|SD|$), as:

$$|SD| = \sqrt{(X - C_x)^2 + (Y - C_y)^2} \tag{3.7}$$

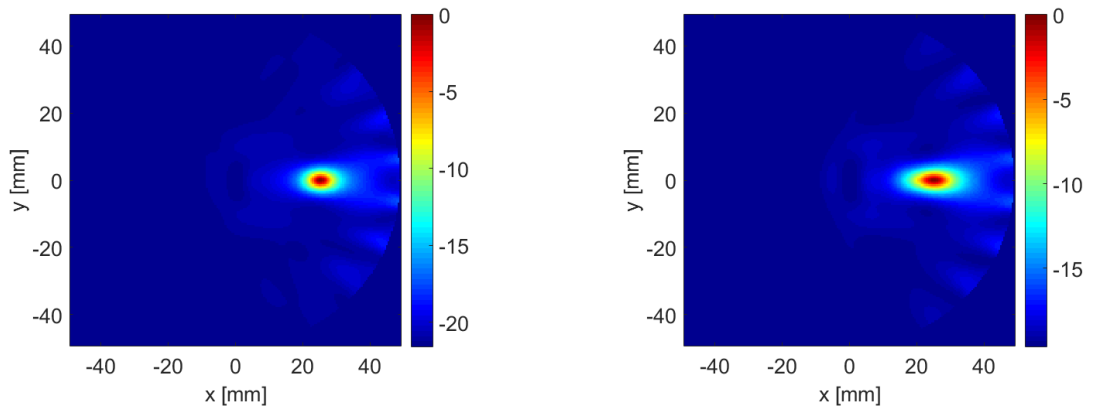

(a) GM-MUSIC: known parameters.

(b) Eye-GMMUSIC: unknown parameters

Figure 3.17: The resulting GM-MUSIC pseudospectra at $\nu = [2, 4]$GHz. (a) The outcome from normal GM-MUSIC process with necessary a priori parameter information. (b) The outcome from Eye-GMMUSIC with no a priori information. Barcolor: from red color, high value in dB, to blue, low values.

we can define a new measure of comparison: the Spatial Displacement Ratio (SDR), writes as

$$SDR = \frac{|SD|_{GM}}{|SD|_{Eye}} \tag{3.8}$$

This measure provides an index of the error committed by Eye-GMMUSIC, compared to the GM-MUSIC error. The results are shown in figure 3.15. The localization performance of Eye-GMMUSIC are lower than GMMUSIC at increasing of the tumor size and at decreasing of the tumor-background contrast. In over 50% of the cases, the Eye-GMMUSIC algorithm returns the same outcome of the GMMUSIC.

Table 3.15: The SDR metric: the error committed by Eye-GMMUSIC ($|SD|_{Eye}$) compared to the GM-MUSIC error($|SD|_{GM}$).

	$\|SD\|_{GM}$[mm]	$\|SD\|_{Eye}$[mm]	SDR
near center	1 ± 1	1 ± 1	1
half radius	1 ± 1	1 ± 1	1
near skin	4 ± 1	4 ± 1	1
small tumor	1 ± 1	1 ± 1	1
med. tumor	1 ± 1	6 ± 1	0.2
large tumor	1 ± 1	9 ± 1	0.1
high contrast	1 ± 1	1 ± 1	1
med. contrast	1 ± 1	2 ± 1	0.5
low contrast	1 ± 1	6 ± 1	0.2
small breast	1 ± 1	1 ± 1	1
med. breast	1 ± 1	3 ± 1	0.3
large breast	1 ± 1	3 ± 1	0.3

The results of Eye-GMMUSIC are not to be considered as negative results, since no a priori information on the breast properties is required. Moreover, we don't forget that a small error on the parameter estimation produces a large delocalization, see § 3.2.6. Under these considerations, the Eye-GMMUSIC can be an efficient tool when there is uncertainty on the parameter estimation.

The results of Eye-GMMUSIC are positive since the medium is perfectly homogeneous, but in the future the algorithm can be modified for a inhomogeneous medium and then become a robust instrument to do microwave imaging without knowing the breast anatomy.

Chapter 4

Experimental Measurements

The analysis carried out on the simulations has the aim to investigate the physics problem under test, to provide the theoretical basis of an operating experimental setup and at last to validate the experimental data.

This Chapter presents the experimental setup built through the guidelines from the simulations. The imaging algorithm is applied to the experimental measurements and the results are compared with the simulated ones. Finally, we reconstruct the images with the Eye-GMMUSIC algorithm and verify its operation on the experimental data.

4.1 The experimental setup

The experimental setup includes the breast phantom, the measuring system and the graphical interface. The the breast phantom, called ARCHIMEDE, is the first phantom prototype built at the University of Bologna. The measuring system is composed by the dipole antenna ANT-24G-905-SMA developed by RF Solutions and the Copper Mountain - S5048 Vector Network Analyzer. The data is read via the PC on which the Copper Mountain software is installed. The figure 4.1 shows the experimental setup.

4.1.1 The breast phantom

The breast phantom consists of three main elements: the breast, the skin layer and the tumor. The breast is a cylindrical plastic tube, its radius is $r_b = 55$mm, its height is $h_b = 500$mm and it is filled with seed oil characterized by relative permittivity ε_b=2. The seed oil simulates the breast adipose tissue. The cylinder can rotate around a vertical axis, it is supported by an upper wood structure and by a fixed circular guide at the bottom. On the upper wood structure, there is a goniometric indicator used to read the angle of rotation. The wall of the tube represents a skin layer with thickness $t_s = 2$mm and unknown electrical parameters. The target to be detected (tumor) is a cylindrical plastic tube with radius $r = 15$mm, its height is $h = h_b$, it is filled with water characterized by ε=80 and it is located at point $\boldsymbol{X}$ with respect to the center of the breast. The phantom is embedded in a coupling medium with $\varepsilon_d = \varepsilon_b$. The phantom prototype, called

(a) Experimental Setup

(b) ARCHIMEDE

(c) Vectror Network Analyzer

(d) Dipole Antenna

Figure 4.1: (a) The experimental setup: (b) the breast phantom ARCHIMEDE, (c) the Vector Network Analyzer (VNA), (d) the dipole antenna.

ARCHIMEDE, is built at University of Bologna , Fig. 4.1b. In figure 4.2 the ARCHIMEDE 2D geometry is synthesized.

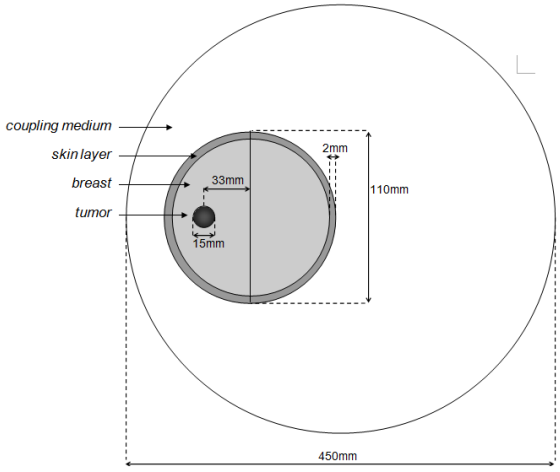

Figure 4.2: Breast phantom geometry: the breast, skin layer and tumor.

4.1.2 The dipole antenna

The antenna used is and half-wave dipole antenna, it is fixed on the upper wood support of ARCHIMEDE phantom and it can be located at three different distances from the breast.

A half-wave dipole antenna consists of two quarter-wavelength conductors placed end to end for a total length of approximately $L = \lambda/2$, Figure 4.3a. The current

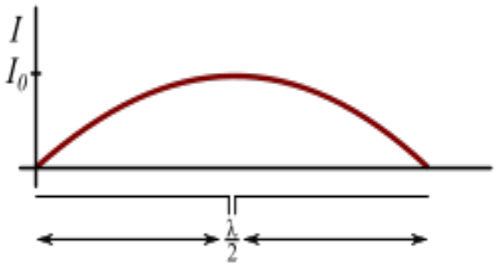

(a) The magnitude of current in a standing wave along the dipole.

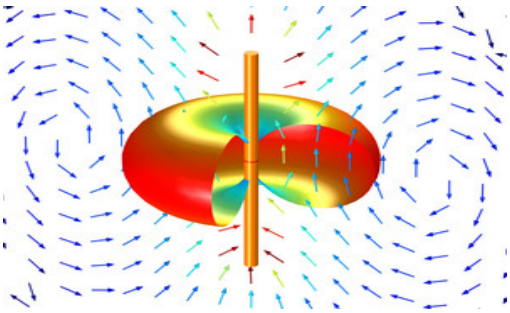

(b) Radiation pattern of a half-wave dipole antenna. Barcolor: from red color, high value in dB, to blue, low values.

Figure 4.3: Current magnitude and radiation pattern of an half-wave dipole antenna.

distribution is that of a standing wave, approximately sinusoidal along the length of the dipole, with a node at each end and an antinode (peak current) at the center (feedpoint):

$$I(z) = I_0 \cdot e^{i\omega t} \cdot \cos kz, \qquad -L/2 \leq z \leq L/2 \tag{4.1}$$

where $\omega = 2\pi f$ is the radian frequency and $k = 2\pi\lambda$ is the wavenumber. In the far field, the electric field pattern at a distance r in the direction θ from the antenna's

axis, is given by [46]:

$$E_\theta = \frac{-iZ_0 I_0}{2\pi r} \cdot \frac{\cos\left(\frac{\pi}{2}\cos\theta\right)}{\sin\theta} \cdot e^{i(\omega t - kr)}. \tag{4.2}$$

where $Z_0 = 1/c\varepsilon_0$ is the impedance of free space and the feedpoint current is assumed to be $I_0 e^{i\omega t}$. The term $\cos[(\pi/2)\cos\theta]/\sin\theta$ is called directional factor. An example of a dipole radiation pattern is shown in Figure 4.3b.

ANT-24G-905-SMA Dipole antenna

The dipole antenna used is the ANT-24G-905-SMA antenna (Fig. 4.1d) developed by RF Solutions. It is an omni-directional gain antenna, its specifications are:

- Frequency Group: 2.4 - 2.5 GHz
- Active gain: +5dB
- Vertical Polarization
- Internal/External usage
- Adjustable 90deg SMA Connector.

4.1.3 Vector Network analyzer

A Vector Network Analyzer (VNA) is the basic measurement instrument used to measure frequency dependent electrical properties of a device under test (DUT). This measurement is typically performed in a broad frequency range, starting from tens of kHz and reaching even hundreds of GHz [47]. The electrical properties are related to the ratios of incident, reflected and transmitted signals (waves) and hence impedance and admittance of the DUT. These ratios are usually expressed in terms of scattering or S-parameters. Figure 4.4 illustrates a two-port device under test.

For a generic multi-port network, the ports are numbered from 1 to N, where N is the total number of ports. For port n, the associated S-parameter definition is in terms of incident and reflected 'power waves', a_n, and b_n, respectively. Kurokawa [48] defines the incident power wave for each port as:

$$a = \frac{1}{2}\, k(V + ZI) \tag{4.3}$$

and the reflected wave for each port is defined as

$$b = \frac{1}{2}\, k(V - Z^* I) \tag{4.4}$$

where Z, is the diagonal matrix of the complex reference impedance for each port and Z^* is the complex conjugate, V and I are respectively the column vectors of the voltages and currents at each port and k is defined as:

$$k = \left(\sqrt{|\mathfrak{Re}\{Z\}|}\right)^{-1} \tag{4.5}$$

S-parameters are simply ratio measurements of the incident wave voltage to the transmitted and reflected wave voltages. Formally, a single element of the S-parameter matrix can be determined as

$$S_{ij} = \left.\frac{b_i}{a_j}\right|_{a_k=0} \qquad \forall k \neq j \tag{4.6}$$

This means that S_ij is measured by driving port j with an RF source to produce an incident wave a_j, and measuring the wave b_i that enters port i. Simultaneously the incident waves on all other ports except the j-th port should be set to 0, therefore, all other ports should be terminated in matched loads to avoid reflections [49]. A device with two ports is characterized by four S-parameters: two reflection coefficients,

$$S_{11} = \left.\frac{b_1}{a_1}\right|_{a_2=0} \qquad S_{22} = \left.\frac{b_2}{a_2}\right|_{a_1=0} \tag{4.7}$$

and two transmission coefficients:

$$S_{12} = \left.\frac{b_1}{a_2}\right|_{a_1=0} \qquad S_{21} = \left.\frac{b_2}{a_1}\right|_{a_2=0}. \tag{4.8}$$

The parameters S_{11} and S_{22} are called reflection coefficients; because they are the ratio of the incident wave amplitude to the amplitude of the resultant wave reflected back to the incident port. S_{12} and S_{21} are called transmission coefficients; because they are the ratio of the incident wave amplitude at one port to the amplitude of the resultant wave transmitted to the opposite port.

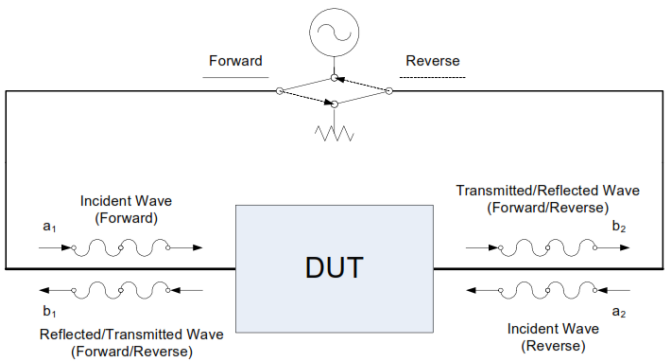

Figure 4.4: A schematized two port VNA: signal diagram of an S-parameter measurement [50].

It can be seen in Figure 4.4 that a two port, full S-parameter, VNA uses a single RF source that is switched between port 1 and port 2. This single source is used to create the incident a waves, which are used as the reference signals in determining the S-parameters. Because there is only one source, and because S-parameters are defined as having only one port driven at a time, a two port VNA is said to have a forward and reverse state. In the forward state, port 1 is driven by the RF source, and an incident wave is produced at this port while port 2 is terminated; during this state S_{11} and S_{21} are measured. In the reverse state, port 2 is driven by the source and an incident wave is produced at port 2 while port 1 is terminated during this S_{22} and S_{12} are measured [50].

Copper Mountain - S5048 VNA

We use the S5048 VNA (Fig. 4.1c) developed by Copper Mountain Technologies. The highly compact S5048 VNA is a 4.8 GHz, 2-port instrument, capable of 120 dB dynamic range and designed for operation with PC. The key features are:

- Frequency range: 20 kHz - 4.8 GHz
- Measured parameters: S_{11}, S_{12}, S_{21} and S_{22}
- Wide output power adjustment range: -50 dBm to +5 dBm
- 123 dB dynamic range (10 Hz IF bandwidth)
- Measurement time per point: 200 μs per point
- Up to 200,001 measurement points
- Multiple precision calibration methods and automatic calibration

4.1.4 PC and Software

The VNA is connected to the computer via USB and delivers accurate testing and measurement through a platform that can keep up with constant advancements as well as be remotely accessed. The graphical interface is the software distributed by the manufacturer: Copper Mountain Software. It allows to measure the S-parameters in the frequency range 20 kHz - 4.8 GHz. The parameters can be measured as complex values (module and phase), but are also expressed as gain in decibel, write as:

$$g = 20 \cdot \log_{10} S_{ij} \tag{4.9}$$

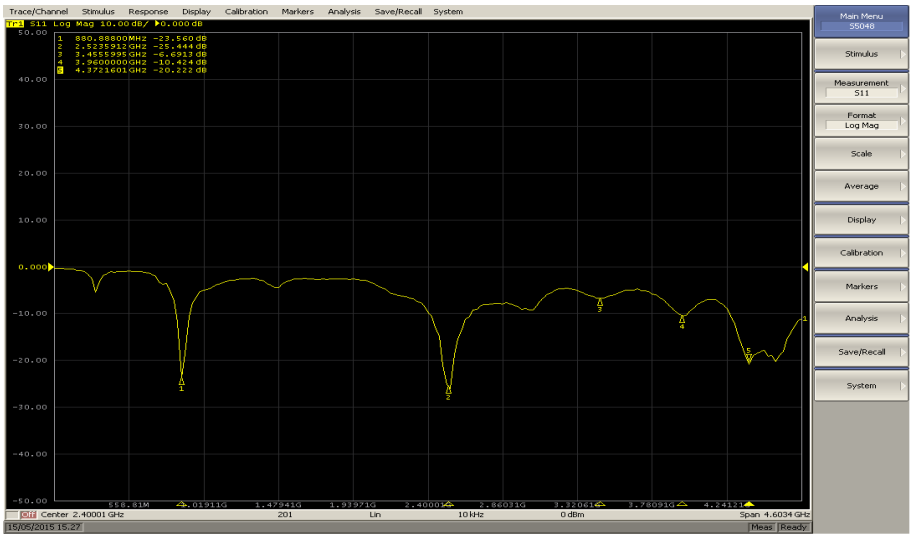

Figure 4.5: Copper Mountain Main Menu. The trace in the graph is the Log Mag (gain signal) of S_{11} collect by the antenna ANT-24G-905-SMA, in air medium with water scatterer.

In Figure 4.5 a screenshot of the software main menu is shown:

- Stimulus: sets the frequency range and step
- Measurement: sets the type of signal: S_{11}, S_{12},S_{21}, S_{22}
- Scale: sets the scale type: Log Mag (g-signal in decibel), phase, real, imag, polar
- Average: average smoothing function

- Display: sets the number of graph in display
- Calibration: VNA calibration menu
- Markers: sets marker in graph
- Save/Recall:
- System: system information

4.2 Measures in air

As preliminary analysis we have acquired measurements in air, $\varepsilon_b = 1$. These measures allow us to test the acquisition system under known conditions, also they are a useful for comparison when the medium is changed.

Consider the breast phantom geometry in § 4.1.1, as described, the antenna is fixed, while the cylindrical tube which represents the breast is rotated. This configuration represents an apparent rotation of the antennas, while the the breast is still. Made this assumption, the S_{11} signal is collected from N=18 antenna positions. The positions occupied by the antenna are equally spaced along a concentric circle with the breast and with radius $r_{ap} = 68$mm, thus, the breast-antenna distance is equal to 13mm. The scatterer is filled of water, $\varepsilon = 80$. The electric parameter contrast between scatter and the breast medium is very high, $\varepsilon : \varepsilon_b = 80 : 1$. The high contrast produces a signal with high gain (fig. 4.7), this enables us to select other frequencies of the spectrum in addition to the resonance frequency. We select different frequencies in order to use the GM-MUSIC algorithm. The working frequencies are selected in the range $\nu = [1, 4]$GHz. Some pseudospettra obtained in the selected frequency range are shown in Figure 4.6.

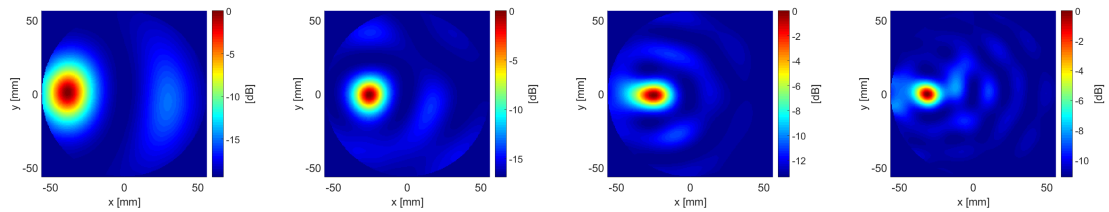

(a) ν=1.2[GHz] **(b)** ν=1.9[GHz] **(c)** ν=3.3[GHz] **(d)** ν=4.1[GHz]

Figure 4.6: Pseudospectra frequency evolution in air, from ν=1[GHz] to ν=4[GHz]. Barcolor: from red color, high value in dB, to blue, low values.

The spatial and contrast metrics are shown in Tab. 4.1, these values are the mean and standard error computed on different measures. We deduce that the experimental results in air follows the guideline achieved with simulations: at low frequencies we have large FWHM, large delocalization and high contrast, while at high frequencies we have small FWHM, good localization, but less contrast due to artifacts. In addition, the experimental results confirm a better scatterer localization in angular direction. The best frequency range is $\nu = [2, 4]$GHz, known result by simulations and confirmed by experimental measures.

We have computed the GM-MUSIC pseudospectrum combining single frequency pseudospectra in the frequency range $\nu = [2, 4]$GHz, Figure 4.10. The resulting metrics are reported in Table 4.3. The GM-MUSIC has lower contrast, smaller

Table 4.1: Spatial and Contrast Metrics as a function of frequency.

	Spatial metrics						Contrast metrics	
ν[GHz]	FWHM$_\rho$[mm]	SD$_\rho$[mm]	p-value$_\rho$	FWHM$_\phi$[mm]	SD$_\phi$[mm]	p-value$_\phi$	SCR[dB]	SCMR[dB]
1.0	21 ± 2	5 ± 1	0.55	17 ± 2	-0.2 ± 0.5	0.98	9 ± 2	5 ± 1
2.0	20 ± 2	1 ± 1	0.96	16 ± 1	0.0 ± 0.5	0.99	10 ± 3	5 ± 1
3.0	15 ± 1	2 ± 1	0.72	13 ± 1	0.1 ± 0.7	0.98	9 ± 3	4 ± 1
4.0	15 ± 2	-2 ± 1	0.78	11 ± 1	0.0 ± 0.5	0.99	8 ± 2	3 ± 1

FWHM and better scatterer localization than the single-frequency case. Even for the experimental data in the air we can conclude that the GM-MUSIC provides better results of the single frequency pseudospectrum.

4.3 Measures in oil

After making preliminary measures in air, we fill the ARCHIMEDE phantom with seed oil. In order to analyze the effects of the new medium, we compare the S_{11} signals produced by the scatterer of water, in oil and in air, as can be seen in Figure 4.7.

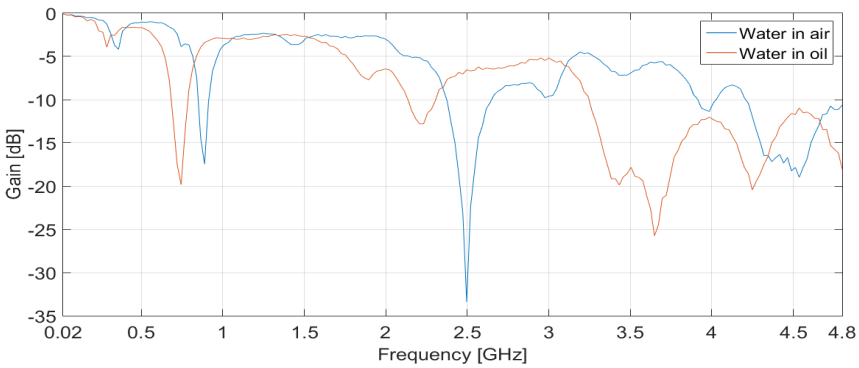

Figure 4.7: S_{11} gain signal as a function of frequency. Red line: water scatterer in air, red line: water scatterer in oil.

The S_{11} spectrum of the water scatterer in oil is weaker than the spectrum in the air and it is shifted to lower frequencies, it occurs because:

$$\varepsilon_{oil} > \varepsilon_{air} \tag{4.10}$$

and this implies:

$$k_{oil} = \frac{2\pi\nu\sqrt{\varepsilon_{oil}}}{c} > \frac{2\pi\nu\sqrt{\varepsilon_{air}}}{c} = k_{air}. \tag{4.11}$$

Consider the breast phantom geometry in § 4.1.1. The S_{11} signal is collected from N=18 antenna positions, equally spaced along a circle concentric with the breast and with radius $r_{ap} = 68$mm. The permittivity of the considered seed oil is unknown, by reference [51] we know that it can vary from $\varepsilon_b = 2$ to $\varepsilon_b = 3$. Knowing the position of the scatterer, we solve the direct problem: we reconstruct with different ϵ_b and test for which epsilon the scatterer is accurately resolved.

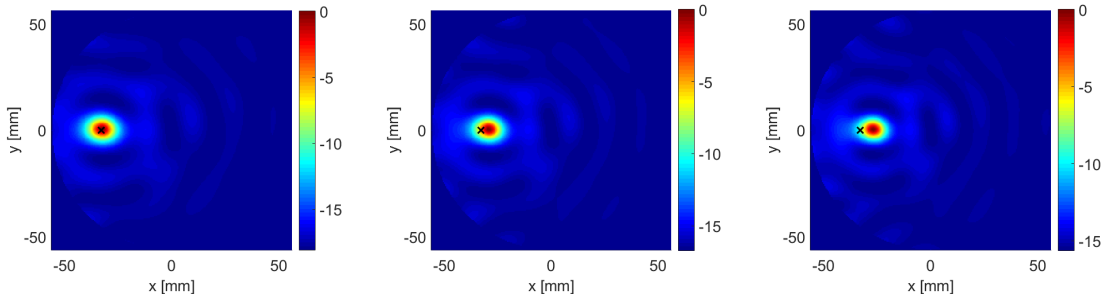

(a) ε_b=2 **(b)** ε_b=2.5 **(c)** ε_b=3

Figure 4.8: The resulting pseudospectra at $\nu = 3$GHz as a function of ε_b. The black cross indicates the true scatterer position. Barcolor: from red color, high value in dB, to blue, low values.

As we can see from figure 4.8, the accurate localization is for ε_b=2. This value does not represent the electrical properties of the breast adipose tissue, in the future it will have to be replaced with a more suitable medium, as castor oil.

The electric parameter contrast between water scatter and the oil medium is $\varepsilon : \varepsilon_b = 80 : 2$, thus we have high contrast and we can select other frequencies of the spectrum in addition to the resonance frequency, and after we compute the GM-MUSIC pseudospectrum. The working frequencies are selected in the range $\nu = [1, 4]$GHz. Some pseudospettra obtained in the selected frequency range are shown in Figure 4.9.

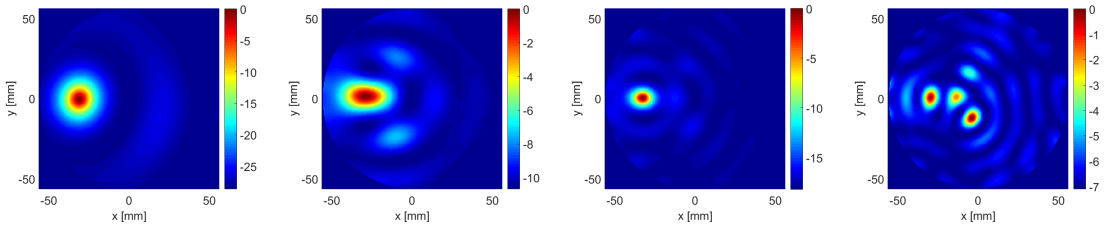

(a) ν=1.2[GHz] **(b)** ν=1.9[GHz] **(c)** ν=3.3[GHz] **(d)** ν=4.1[GHz]

Figure 4.9: Pseudospectra frequency evolution in oil, from ν=1[GHz] to ν=4[GHz]. Barcolor: from red color, high value in dB, to blue, low values.

The spatial and contrast metrics are shown in Tab. 4.2. The values listed are the mean and standard error computed on different measures. The viscous medium disrupts the signal at high frequencies, the artifact created to 4GHz has greater value than the true signal, this situation is deceitful, therefore it must be avoided. On the other hand the reconstructions at low frequencies are improved comparing to those in air. The frequency range for that produces a useful reconstruction is $\nu = [1.5, 3.5]$GHz. In this frequency range, the experimental results in the oil are similar to air: although the scatter-medium contrast is halved, it remains very high (40:1).

We have computed the GM-MUSIC pseudospectrum combining single frequency pseudospectra in the frequency range $\nu = [1.5, 3.5]$GHz, see Figure 4.10. The resulting metrics are reported in Table 4.3. The GM-MUSIC has lower contrast and larger FWHM, but it has better scatterer localization than the single-frequency

Table 4.2: Spatial and Contrast Metrics as a function of frequency.

	Spatial metrics						Contrast metrics	
ν[GHz]	FWHM$_\rho$[mm]	SD$_\rho$[mm]	p-value$_\rho$	FWHM$_\phi$[mm]	SD$_\phi$[mm]	p-value$_\phi$	SCR[dB]	SCMR[dB]
1.0	15 ± 2	- 2 ± 1	0.74	14 ± 2	-0.2 ± 0.5	0.98	17 ± 2	7 ± 1
2.0	24 ± 2	- 4 ± 1	0.70	13 ± 1	0.0 ± 0.5	0.99	7 ± 3	4 ± 1
3.0	11 ± 1	1 ± 1	0.93	9 ± 1	0.1 ± 0.7	0.98	13 ± 3	6 ± 1
4.0	21 ± 2	-22 ± 1	0.02	9 ± 1	11 ± 5	0.05	5 ± 5	1 ± 1

case. The GM-MUSIC has a better scatterer location than the single-frequency case, even in oil.

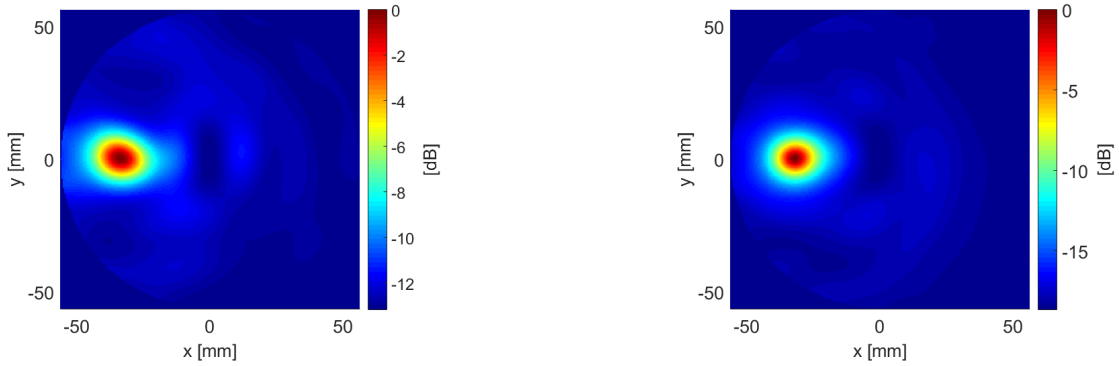

(a) GM-MUSIC in air medium **(b)** GM-MUSIC in oil medium

Figure 4.10: The resulting GM-MUSIC pseudospectra obtained in air and oil mediums with water scatterer. Frequency range $\nu = [1.5, 3.5]$GHz. Barcolor: from red color, high value in dB, to blue, low values.

Table 4.3: Spatial and contrast metrics for GM-MUSIC pseudospectra in oil with water and alcohol scatterers.

	Spatial metrics						Contrast metrics	
	FWHM$_\rho$[mm]	SD$_\rho$[mm]	p-value$_\rho$	FWHM$_\phi$[mm]	SD$_\phi$[mm]	p-value$_\phi$	SCR[dB]	SCMR[dB]
air med.	18 ± 2	2 ± 1	0.91	14 ± 2	-0.1 ± 0.8	0.99	9 ± 5	4 ± 2
oil med.	15 ± 2	-2 ± 1	0.71	12 ± 2	-0.1 ± 0.8	0.99	12 ± 5	4 ± 2

The metrics in oil medium are better than ones in air. This is a direct consequence of the fact that in the oil medium the wavelength is shorter than in the air one, therefore we have a better spatial resolution. Moreover, in oil medium, due the greater conductivity than in the air one, the signal is attenuated and less affected by external interference, therefore we have better SCR and SCMR.

4.3.1 Measure in oil with alcohol scatterer

In order to get closer to a clinical experimental condition, we fill the scatter embedded in ARCHIMEDE phantom with a mixture of ethyl alcohol (90%) and water. The permittivity of ethyl alcohol mixture is equal to $\varepsilon = 31$, by reference [52]. Now, the background-scatterer contrast is $\varepsilon : \varepsilon_b = 15 : 1$. We compute the GM-MUSIC pseudospectrum in the frequency rage $\nu = [1.5, 3.5]$GHz.

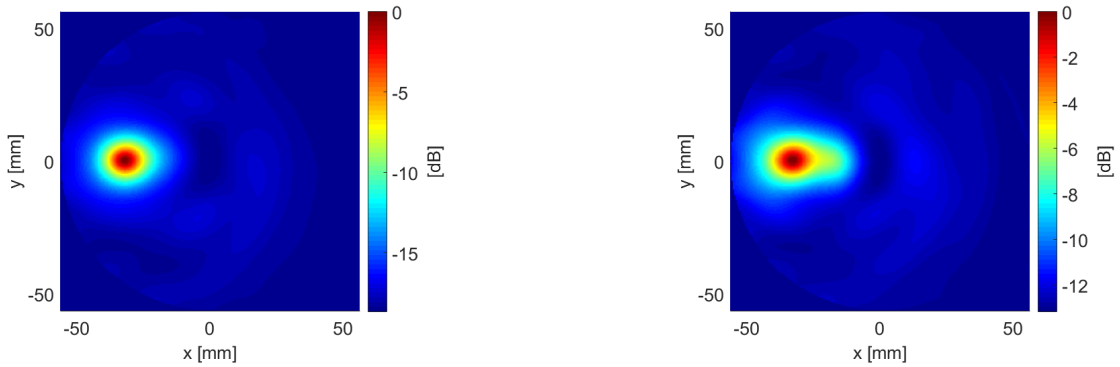

(a) GM-MUSIC with water scatterer **(b)** GM-MUSIC with alcohol scatterer

Figure 4.11: The resulting GM-MUSIC pseudospectra obtained in oil medium with water and alcohol scatterers. Frequency range $\nu = [1.5, 3.5]$GHz. Barcolor: from red color, high value in dB, to blue, low values.

Table 4.4: Spatial and contrast metrics for GM-MUSIC pseudospectra in oil medium with water and alcohol scatterers.

	Spatial metrics						Contrast metrics	
	FWHM_ρ[mm]	SD_ρ[mm]	p-value_ρ	FWHM_ϕ[mm]	SD_ϕ[mm]	p-value_ϕ	SCR[dB]	SCMR[dB]
water scatt.	15 ± 2	-2 ± 1	0.71	12 ± 2	-0.1 ± 0.8	0.99	12 ± 5	4 ± 2
alcohol scatt.	17 ± 2	-2 ± 1	0.87	12 ± 2	-0.1 ± 0.8	0.99	7 ± 5	3 ± 2

Figure 4.11 shows the GM-MUSIC pseudospectra computed with water scatterer and alcohol scatterer in oil, while Table 4.4 compares the metrics. The contrast scatterer-background reduction causes a loss resolution, we note a deformation of signal area in the pseudospectrum with an higher value of FWHM_ρ and also we note a loss in contrast, in particular a large decrease of the SCR metric.

4.4 Eye-GMUSIC Results

In this section the experimental data obtained in three configurations, air medium with water scatterer, oil medium with water scatterer and oil medium with alcohol scatterer, are reconstructed using the Eye-GMMUSIC algorithm described in § 3.3.

Table 4.5: The SDR metric: the error committed by Eye-GMMUSIC ($|SD|_{Eye}$) compared to the GM-MUSIC error($|SD|_{GM}$).

	$\lvert SD\rvert_{GM}$[mm]	$\lvert SD\rvert_{Eye}$[mm]	SDR
air med. with water scatt.	2 ± 1	6 ± 1	0.3
oil med. with water scatt.	2 ± 1	3 ± 1	0.7
oil med. with alcohol scatt.	2 ± 1	5 ± 1	0.4

The results of Eye-GMMUSIC for experimental data are worse than those obtained with GMMUSIC. This occurs because the algorithm implementation is based on the simulations data, which have higher precision than the experimental ones. The noise signal in experimental data is higher than in simulation ones, thus

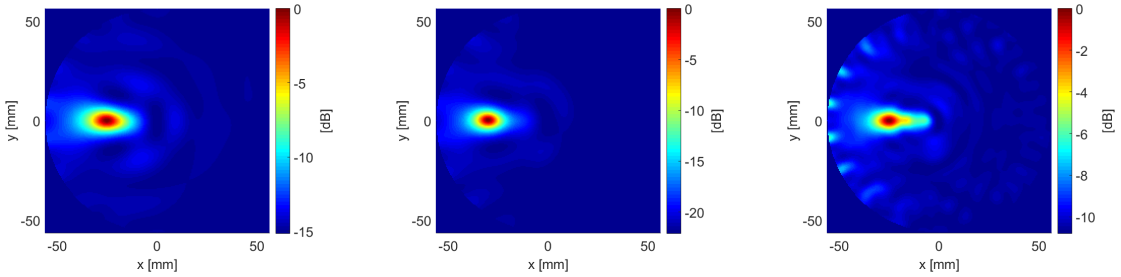

(a) Air medium with water scatterer

(b) Oil medium with water scatterer

(c) Oil medium with alcohol scatter

Figure 4.12: Eye-GMMUSIC Pseudospectra in each experimental configuration, frequency range $\nu = [1.5, 3.5]$GHz. Barcolor: from red color, high value in dB, to blue, low values.

the optimization algorithm have to search the absolute minimum in a parameter space with a lot of local minima. In Figure 4.13 are compared the cost function convergences of the simulations and experimental data. The cost function convergence of the experimental data is slower than the simulated one, it takes place after about 150 iterations, also we note the presence of plateaus that stretches the computation time.

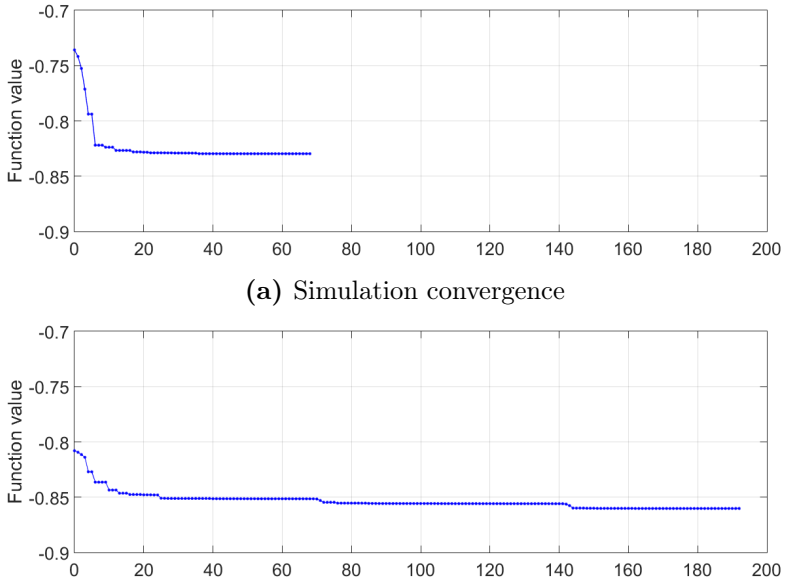

(a) Simulation convergence

(b) Experimental convergence

Figure 4.13: Const function convergence as a function of iterations. Top: cost function convergence for the simulation data. Bottom: cost function convergence for the experimental data.

Chapter 5

Conclusions

The use of microwave imaging for breast-cancer detection has been investigated. Study of the literature suggests that a contrast in the electromagnetic constitutive parameters exists at microwave frequencies between the healthy and the cancerous breast tissue. This implies that an incident microwave field will scatter if a tumor is present and microwave imaging may therefore be used for screening for breast cancer.

In this thesis, the problem of localizing a scatterer, which represents a tumor, in a homogeneous circular domain, which represents a breast, is addressed. This problem formulation implies the solution of the electromagnetic inverse scattering problem. The solution is found implementing an algorithm based on a linear procedure solution, inspired by MUltiple SIgnal Classification algorithm (MUSIC) and Time Reversal method (TR). The algorithm returns a reconstructed image of the investigation domain in which it is detected the scatterer position. This image is called pseudospectrum.

A preliminary performance analysis of the algorithm varying the working frequency is performed. The algorithm resolution performance increases with frequency, whilst the signal-to-noise ratio increases up to 4GHz, then decreases. In addition, the results shows a better scatterer localization in angular direction than radial one. The frequency range from $\nu = 2$GHz to $\nu = 4$GHz is selected as trade-off between resolution and signal-to-noise contrast. Then, the performance of the algorithm are improved combining the pseudospectra obtained at single-frequency. The Geometrical Mean-MUSIC algorithm (GM- MUSIC) is proposed as multi-frequency method.

The performance of the GM-MUSIC is tested in different computer simulations varying the following parameters: tumor position, tumor size, breast dimension, background-scatterer contrast. The algorithm has excellent performance in changing the physical size of the breast or the scatterer, the results degrade when the contrast between the electrical parameters of the breast and the scatterer decreases and the scatterer localization fails when estimating the electrical parameters of the breast is incorrect. This is an evident limit, since, in a real life situation, the anatomy of the breast is unknown. For these reasons, our analysis focuses on the problem estimation of the breast electric parameters.

An improvement in GM-MUSIC is proposed: the Eye-GMMUSIC algorithm.

Eye-GMMUSIC algorithm needs no a priori information on the electrical parameters of the breast. It is an optimizing algorithm based on the pattern search algorithm: it searches the breast parameters which minimize the Signal-to-Clutter Mean Ratio (SCMR) in the signal. In over 50% of the analyzed cases, the Eye-GMMUSIC algorithm returns the same outcome of the GMMUSIC, while in other cases it returns a comparable solution.

Finally, the GM-MUSIC and the Eye-GMMUSIC algorithms are tested on a microwave breast cancer detection system consisting of an dipole antenna, a Vector Network Analyzer and a breast phantom built at University of Bologna. The scatterer medium and the breast medium are changed in the phantom, so three system configurations are considered: water scatterer embedded in air medium, water scatterer in oil medium and alcohol scatterer in oil medium. The reconstructions of experimental data suggest that a better frequency range is from $\nu = 1.5$GHz to $\nu = 3.5$GHz. In this frequency range the reconstructions of experimental data follow the guideline of simulation ones. In alcohol scatterer in oil medium configuration, the scatterer-background contrast reduction causes a loss resolution and a loss in contrast. We recommend the use of an antenna with greater gain if the electric contrast is further decreased.

The results of Eye-GMMUSIC for experimental data are lower than those obtained with GMMUSIC. This occurs because the algorithm implementation is based on the simulations data, which have higher precision than the experimental ones. In the future, we could change the optimizing algorithm or better estimate the parameters on which the optimization algorithm is based, as the estimation of Signal-to-Clutter Mean Ratio.

Future work

The extension of this work will be the scatterer localization in an inhomogeneous medium. In the future, areas with different medium could be embedded in the breast phantom, this areas will represent fibroglandular breast tissue. It will be important to distinguish a tumor scatterer from fibroglandular one, through specific filtering methods. The final goal of the 2-D reconstructions will be the detection of a tumor embedded in a real-like phantom slice.

Appendix A

Green function

In mathematics, a Green's function is the impulse response of an inhomogeneous differential equation defined on a domain, with specified initial conditions or boundary conditions. Given a linear differential operator L_x acting on the collection of distributions over a subset Ω of some Euclidean space $\mathbb{R}^n$, a Green's function $G(x, y)$ at the point y in Ω corresponding to L_x is any solution of:

$$L_x G(x, y) = \delta(x - y). \tag{A.1}$$

where δ denotes the delta function. Thanks to the properties of the Dirac delta function, we can write:

$$f(x) = \int f(y)\delta(x - y)dy = \int f(y)L_x G(x, y)dy, \tag{A.2}$$

being $f(x) = L_x u(x)$, we have:

$$L_x u(x) = L_x \int f(y)G(x, y)dy \quad \Rightarrow \quad u(x) = \int f(y)G(x, y)dy + q(x) \tag{A.3}$$

where $q(x)$ is a solution of the associated homogeneous equation $L_x q(x) = 0$. The arbitrary function $q(x)$ is uniquely determined by the boundary conditions of the problem.

Appendix B

Hankel function

In mathematical analysis the Hankel functions are the third kind Bessel functions. The Bessel functions (cylindrical harmonics) are canonical solutions $y(x)$ of the linear second-order ordinary differential equation given by:

$$x^2y'' + xy' + (x^2 + \alpha^2)y = 0 \tag{B.1}$$

where α is called the order of the equation, while $x, y \in \mathbb{C}$. The solution of the ordinary equation can be sought in the general form:

$$y(x) = \sum_{n=0}^{\infty} a_n x^{n+b} \tag{B.2}$$

First kind of Bessel function.

If the order is not the integer ($\alpha \notin \mathbb{N}$) the general solution of (B.1) can be expressed in the form:

$$y(x) = C_1 J_\alpha(x) + C_2 J_{-\alpha}(x) \quad C_1, C_2 \in \mathbb{R} \tag{B.3}$$

where:

$$\begin{aligned} J_\alpha(x) &= \left(\frac{x}{2}\right)^\alpha \sum_{n=0}^{\infty} \frac{(-1)^n (\frac{x}{2})^{2n}}{n!\Gamma(\alpha + n + 1)} \\ J_{-\alpha(x)} &= \left(\frac{x}{2}\right)^{-\alpha} \sum_{n=0}^{\infty} \frac{(-1)^n (\frac{x}{2})^{2n}}{n!\Gamma(-\alpha + n + 1)} \end{aligned} \tag{B.4}$$

Second kind of Bessel function.

When α is integer occurs that $\Gamma(\alpha) = (\alpha - 1)!$ and results $J_\alpha(x) = (-1)^\alpha J_{-\alpha}(x)$. In this case the general solution of (B.1) is no longer (B.3), because $J_\alpha(x)$ and $J_{-\alpha}(x)$ are independent, hence it is the Neumann functions $Y_\alpha(x)$, a linear combination of the two opposing Bessel functions:

$$Y_\alpha(x) = \frac{J_\alpha(x)\cos(\alpha\pi) - J_{-\alpha}(x)}{\sin(\alpha\pi)} \tag{B.5}$$

the general solution is:

$$y(x) = C_1 J_\alpha(x) + C_3 Y_{-\alpha}(x) \quad C_1, C_3 \in \mathbb{R}. \tag{B.6}$$

Third kind of Bessel function.

A further formulation of the solution of (B.1) is given by Hankel functions:

$$\begin{aligned} H_\alpha^{(1)}(x) &= J_\alpha(x) + iY_\alpha(x) \\ H_\alpha^{(2)}(x) &= J_\alpha(x) - iY_\alpha(x) \end{aligned} \tag{B.7}$$

whose general solution:

$$y(x) = C_4 H_\alpha^{(1)}(x) + C_5 H_\alpha^{(2)}(x) \quad C_4, C_5 \in \mathbb{R}. \tag{B.8}$$

These functions are used to express solutions of equations of cylindrical wave propagating respectively outside and inside of the cylinder.

Spherical Hankel function.

When solving the Helmholtz equation in spherical coordinates by separation of variables, the radial equation has the form:

$$x^2 y'' + 2xy' + (x^2 - n(n+1))y = 0 \tag{B.9}$$

The two linearly independent solutions to this equation are called the spherical Bessel functions j_n and y_n, and are related to the ordinary Bessel functions J_n and Y_n by:

$$\begin{aligned} j_n(x) &= \sqrt{\frac{\pi}{2x}} J_{n+\frac{1}{2}}(x), \\ y_n(x) &= \sqrt{\frac{\pi}{2x}} Y_{n+\frac{1}{2}}(x) = (-1)^{n+1} \sqrt{\frac{\pi}{2x}} J_{-n-\frac{1}{2}}(x). \end{aligned} \tag{B.10}$$

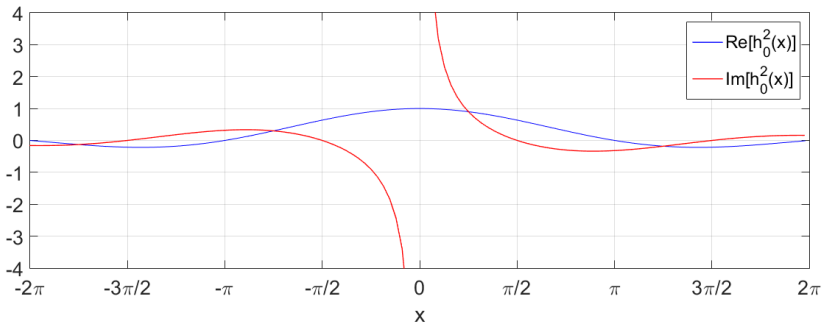

Figure B.1: The real and imaginary part of the Hankel function of second kind and zero order.

The spherical Bessel functions can also be written as (Rayleigh's formulas):

$$\begin{aligned} j_n(x) &= (-x)^n \left(\frac{1}{x}\frac{d}{dx}\right)^n \frac{\sin(x)}{x}, \\ y_n(x) &= -(-x)^n \left(\frac{1}{x}\frac{d}{dx}\right)^n \frac{\cos(x)}{x}. \end{aligned} \tag{B.11}$$

There are also spherical analogues of the Hankel functions:

$$\begin{aligned} h_n^{(1)}(x) &= j_n(x) + iy_n(x), \\ h_n^{(2)}(x) &= j_n(x) - iy_n(x). \end{aligned} \tag{B.12}$$

In this thesis we focus on Hankel function of second kind and zero order, writes as:

$$h_0^{(2)}(x) = i\frac{e^{-ix}}{x} = \frac{\sin(x)}{x} - i\frac{\cos(x)}{x} \tag{B.13}$$

As shown in fig. B.1, this function has a discontinuity in $x = 0$.

Bibliography

[1] Jacques Ferlay, Isabelle Soerjomataram, Rajesh Dikshit, Sultan Eser, Colin Mathers, Marise Rebelo, Donald Maxwell Parkin, David Forman, and Freddie Bray. «Cancer incidence and mortality worldwide: sources, methods and major patterns in GLOBOCAN 2012». *International Journal of Cancer,* 136.5: E359-E386 (2015). Wiley Online Library.

[2] Associazione Italiana dei Registri TUMori AIRTUM. «ITACAN: Tumori in Italia, Versione 2.0.» (2014). `http://www.registri-tumori.it`.

[3] Carol DeSantis, Rebecca Siegel, Priti Bandi, and Ahmedin Jemal. «Breast cancer statistics, 2011». *CA: a cancer journal for clinicians,* 2011, 61.6: 408-418 (2011). Wiley Online Library.

[4] Laszlo Tabar and Peter B Dean. «A new era in the diagnosis and treatment of breast cancer». *The breast journal,* 16.s1: S2-S4 (2010). Wiley Online Library.

[5] Phan T Huynh, Amanda M Jarolimek, and Susanne Daye. «The false-negative mammogram.» *Radiographics,* 18.5: 1137-1154 (1998).

[6] Joann G Elmore, Mary B Barton, Victoria M Moceri, Sarah Polk, Philip J Arena, and Suzanne W Fletcher. «Ten-year risk of false positive screening mammograms and clinical breast examinations». *New England Journal of Medicine,* 338.16: 1089-1096 (1998). Mass Medical Soc.

[7] Amy Berrington de González and Sarah Darby. «Risk of cancer from diagnostic X-rays: estimates for the UK and 14 other countries». *The lancet,* 363.9406: 345-351 (2004). Elsevier.

[8] Debra M Ikeda, Douglas R Baker, and Bruce L Daniel. «Magnetic resonance imaging of breast cancer: clinical indications and breast MRI reporting system». *Journal of Magnetic Resonance Imaging,* 12.6: 975-983 (2000). Wiley Online Library.

[9] Wendie A Berg, Lorena Gutierrez, Moriel S NessAiver, W Bradford Carter, Mythreyi Bhargavan, Rebecca S Lewis, and Olga B Ioffe. «Diagnostic accuracy of mammography, clinical examination, US, and MR imaging in preoperative assessment of breast cancer 1». *Radiology,* 233.3: 830-849 (2004). Radiological Society of North America.

[10] John H Jacobi and Lawrence E Larsen. «Microwave interrogation of dielectric targets. Part II: By microwave time delay spectroscopy». *Medical physics,* 5.6: 509-513 (1978). American Association of Physicists in Medicine.

[11] Susan C Hagness, Allen Taflove, and Jack E Bridges. «Two-dimensional FDTD analysis of a pulsed microwave confocal system for breast cancer detection: Fixed-focus and antenna-array sensors». *Biomedical Engineering, IEEE Transactions on* 45.12: 1470-1479 (1998). IEEE.

[12] Xu Li and Susan C Hagness. «A confocal microwave imaging algorithm for breast cancer detection». *Microwave and Wireless Components Letters, IEEE,* 5.6: 509-513 (2001). IEEE.

[13] Susan C Hagness, Allen Taflove, and Jack E Bridges. «Three-dimensional FDTD analysis of a pulsed microwave confocal system for breast cancer detection: Design of an antenna-array element». *Antennas and Propagation, IEEE Transactions on* 47.5: 783-791 (1999). IEEE.

[14] Sverre Grimnes, Oslo Rikshospitalet, and Norway Herman P Schwan. «Interface phenomena and dielectric properties of biological tissue». 20: 2643-2653 (2002).

[15] Camelia Gabriel. «Compilation of the Dielectric Properties of Body Tissues at RF and Microwave Frequencies» (1996).

[16] Camelia Gabriel, Sami Gabriel, and E Corthout. «The dielectric properties of biological tissues: I. Literature survey». *Physics in medicine and biology,* 41.11: 2231 (1996). IOP Publishing.

[17] S Gabriel, RW Lau, and Camelia Gabriel. «The dielectric properties of biological tissues: II. Measurements in the frequency range 10 Hz to 20 GHz». *Physics in medicine and biology,* 41.11: 2251 (1996). IOP Publishing.

[18] Sami Gabriel, RW Lau, and Camelia Gabriel. «The dielectric properties of biological tissues: III. Parametric models for the dielectric spectrum of tissues». *Physics in medicine and biology,* 41.11: 2271 (1996). IOP Publishing.

[19] S S Chaudhary, Chaudhary SS, R K Mishra, Mishra RK, A Swarup, Swarup A, J M Thomas, and Thomas JM. «Dielectric properties of normal & malignant human breast tissues at radiowave and microwave frequencies». *Indian journal of biochemistry & biophysics,* 21.1: 76 (1984).

[20] Andrzej J Surowiec, Stanislaw S Stuchly, J Robin Barr, and AASA Swarup. «Dielectric properties of breast carcinoma and the surrounding tissues». *Biomedical Engineering, IEEE Transactions on,* 35.4: 257-263 (1988). IEEE.

[21] William T Joines, Yang Zhang, Chenxing Li, and Randy L Jirtle. «The measured electrical properties of normal and malignant human tissues from 50 to 900 MHz». *Medical physics,* 21.4: 547-550 (1994). American Association of Physicists in Medicine.

[22] Mariya Lazebnik, Leah McCartney, Dijana Popovic, Cynthia B Watkins, Mary J Lindstrom, Josephine Harter, Sarah Sewall, Anthony Magliocco, John H Booske, Michal Okoniewski, et al. «A large-scale study of the ultrawideband microwave dielectric properties of normal breast tissue obtained from reduction surgeries». *Physics in medicine and biology,* 52.10: 2637 (2007). IOP Publishing.

[23] Mariya Lazebnik, Dijana Popovic, Leah McCartney, Cynthia B Watkins, Mary J Lindstrom, Josephine Harter, Sarah Sewall, Travis Ogilvie, Anthony Magliocco, Tara M Breslin, et al. «A large-scale study of the ultrawideband microwave dielectric properties of normal, benign and malignant breast tissues obtained from cancer surgeries». *Physics in Medicine and Biology,* 52.20: 6093 (2007). IOP Publishing.

[24] Ralph O Schmidt. «Multiple emitter location and signal parameter estimation». *Antennas and Propagation, IEEE Transactions on,* 34.3: 276-280 (1986). IEEE.

[25] Anthony J Devaney. «Super-resolution processing of multi-static data using time reversal and MUSIC». *J. Acoust. Soc. Am* (2000).

[26] Hanoch Lev-Ari and AJ Devancy. «The time-reversal technique re-interpreted: Subspace-based signal processing for multi-static target location». 509-513 (2000). IEEE.

[27] Fred K Gruber, Edwin A Marengo, and Anthony J Devaney. «Time-reversal imaging with multiple signal classification considering multiple scattering between the targets». *The Journal of the Acoustical Society of America* 115.6: 3042-3047 (2004). Acoustical Society of America.

[28] Matteo Pastorino. «Microwave imaging». 208 (2010). John Wiley & Sons.

[29] Paul M Meaney, Keith D Paulsen, Alexander Hartov, and Robert K Crane. «An active microwave imaging system for reconstruction of 2-D electrical property distributions». *Biomedical Engineering, IEEE Transactions on* 42.10: 1017-1026 (1995). IEEE.

[30] Alexandre E Souvorov, Alexander E Bulyshev, Serguei Y Semenov, Robert H Svenson, Alexei G Nazarov, Yuri E Sizov, and George P Tatsis. «Microwave tomography: A two-dimensional Newton iterative scheme». *Microwave Theory and Techniques, IEEE Transactions on* 46.11: 1654-1659 (1998). IEEE.

[31] Panagiotis Kosmas, Jacob D Shea, Barry D Van Veen, and Susan C Hagness. «Three-dimensional microwave imaging of realistic breast phantoms via an inexact Gauss-Newton algorithm». IEEE: 1-4 (2008).

[32] Andreas Fhager, Parham Hashemzadeh, and Mikael Persson. «Reconstruction quality and spectral content of an electromagnetic time-domain inversion algorithm». *Biomedical Engineering, IEEE Transactions on* 53.8: 1594-1604 (2006). IEEE.

[33] Panagiotis Kosmas and Carey M Rappaport. «A matched-filter FDTD-based time reversal approach for microwave breast cancer detection». *Antennas and Propagation, IEEE Transactions on* 54.4: 1257-1264 (2006). IEEE.

[34] Raffaele Solimene, Giuseppe Ruvio, Angela Dell'Aversano, Antonio Cuccaro, Max J Ammann, and Rocco Pierri. «Detecting point-like sources of unknown frequency spectra». *Progress In Electromagnetics Research B,* 50: 347-364 (2013). EMW Publishing.

[35] Giuseppe Ruvio, Raffaele Solimene, Antonio Cuccaro, Domenico Gaetano, Jacinta E Browne, and Max J Ammann. «Breast cancer detection using interferometric MUSIC: Experimental and numerical assessment». *Medical physics* 41.10: 103101 (2014). American Association of Physicists in Medicine.

[36] Giuseppe Ruvio, Raffaele Solimene, Antonietta D'Alterio, Max J Ammann, and Rocco Pierri. «RF breast cancer detection employing a noncharacterized vivaldi antenna and a MUSIC-inspired algorithm». *International Journal of RF and Microwave Computer-Aided Engineering* 23.5: 598-609 (2013). Wiley Online Library.

[37] Giuseppe Ruvio, Raffaele Solimene, Antonio Cuccaro, and Max J Ammann. «Comparison of Noncoherent Linear Breast Cancer Detection Algorithms Applied to a 2-D Numerical Model». *Antennas and Wireless Propagation Letters, IEEE* 12: 853-856 (2013). IEEE.

[38] E. Zastrow, S.K. Davis, M. Lazebnik, F. Kelcz, B.D. Van Veen, and S.C. Hagness. «Database of 3D Grid-Based Numerical Breast Phantoms for use in Computational Electromagnetics Simulations» (2007). `http://uwcem.ece.wisc.edu/phantomRepository.html`.

[39] American College of Radiology. «Breast Imaging Reporting and Data System» (2003).

[40] Ian Jolliffe. «Principal component analysis» (2002). Wiley Online Library.

[41] Olgierd Cecil Zienkiewicz, Robert Leroy Taylor, Olgierd Cecil Zienkiewicz, and Robert Lee Taylor. «The finite element method» (1977). McGraw-hill London.

[42] M.J. Turner and R.W. Clough. «Stiffness and deflection analysis of complex structures». *Journal of the Aeronautical Sciences (Institute of the Aeronautical Sciences),* 23.9 (2012).

[43] Carlos A Felippa. «Introduction to finite element methods». *Course Notes, Department of Aerospace Engineeing Sciences, University of Colorado at Boulder,* (2004). `http://www.colorado.edu/engineering/Aerospace/CAS/courses.d/IFEM.d`.

[44] Robert Hooke and To A Jeeves. «"Direct Search" Solution of Numerical and Statistical Problems». *Journal of the ACM (JACM),* 8.2: 212-229 (1961). ACM.

[45] Virginia Torczon. «On the convergence of pattern search algorithms». *SIAM Journal on optimization,* 7.1: 1-25 (1997). SIAM.

[46] Samuel Silver. «Microwave antenna theory and design» (1949). Iet.

[47] David Marlow Kerns and Robert William Beatty. «Basic theory of waveguide junctions and introductory microwave network analysis» (1967). Pergamon.

[48] Kaneyuki Kurokawa. «Power waves and the scattering matrix». *Microwave Theory and Techniques, IEEE Transactions on* 13.2: 194-202 (1965). IEEE.

[49] David M Pozar. «Microwave engineering» (2009). John Wiley & Sons.

[50] John Edward Daniel. «Development of enhanced multiport network analyzer calibrations using non-ideal standards» (2005). American Studies Commons.

[51] ZH Shah and QA Tahir. «Dielectric properties of vegetable oils». *Journal of Scientific Research* 3.3: 481-492 (2011).

[52] Jeffries Wyman. «The Dielectric Constant of Mixtures of Ethyl Alcohol and Water from-5 to 40». *Journal of the American Chemical Society* 53.9: 3292-3301 (1931). ACS Publications.

[53] Alex Fraser, Donald Burnell, et al. «Computer models in genetics.» *Computer models in genetics.* (1970). New York and London: McGraw-Hill Book Company.

[54] Scott Kirkpatrick, MP Vecchi, et al. «Optimization by simmulated annealing». *science* 220.4598: 671-680 (1983).